Supplementary information

Oxygen species-driven dynamic reconstruction with wide-range valence oscillation boosts CO_2 electroreduction

Hanxia Chen [1]†, Juzhe Liu [1]*†, Peiyuan Du [1], Jinmeng Li [1], Zhouqing Xue [1], Yuheng Wang [1], Xiaoxue Xu [1], Jing Zhang [2], Zhongfei Xu [1]*, Qiangwei Li [1], Guang Mo [2], Yunpeng Liu [2,3]* and Lidong Wang [1]*

[1]MOE Key Laboratory of Resources and Environmental Systems Optimization, College of Environmental Science and Engineering, North China Electric Power University, Beijing, 102206, P. R. China

[2]Institute of High Energy Physics, Chinese Academy of Sciences, Beijing 100049, P. R. China

[3]University of Chinese Academy of Sciences, Chinese Academy of Sciences, Beijing 100049, China

†These authors contribute equally to this work.

*E-mail: liujuzhe@ncepu.edu.cn; xuzhongfei@ncepu.edu.cn; liuyunpeng@ihep.ac.cn; wld@ncepu.edu.cn

This file contains Figures S1-S61 and Tables S1-S4.

Table of Content

Supplementary Experimental

Materials and chemicals

Copper (II) chloride dihydrate ($CuCl_2 \cdot 2H_2O$, ≥99.9%), Ascorbic acid (AA, ≥99.0%) and Sodium citrate were purchased from Shanghai Aladdin Biochemical Technology Co., Ltd. Potassium hydroxide (KOH, ≥95.0%) was purchased from Shanghai Macklin Biochemical Co., Ltd. Polyvinylpyrrolidone (PVP, MW 30000) was obtained from Xilong Scientific Co., Ltd. Nafion solution (5 wt%) was provided by Dupont Company. Ethanol (C_2H_5OH, ≥99.7%) was supplied by Tianjin Fuchen Chemical Reagent Co., Ltd. Deuterium oxide (DMSO, ≥99.9%) was purchased from Innochem. Ni foam and gas diffusion layer (GDL, YLS-30T) were purchased from Suzhou Sinero. CO_2 (≥99.999%), CO (≥99.999%) and Ar (≥99.9999%) were all supplied by Air. Deionized water (18.25 MΩ cm) was used in all experiments. All the chemical reagents were used as received without any further purification.

Synthesis of truncated Cu_2O (t-Cu_2O)

For typical synthesis of t-Cu_2O[1], 1.5 g of PVP was treated by 100 mL of 0.01 M $CuCl_2 \cdot 2H_2O$ solution, followed by addition of 10 mL of 2.0 M NaOH into the mixture. After continuous stirring for 0.5 h, 10.0 mL of 0.6 M AA solution was added dropwise to the resulting blue solution. The mixture was then agitated in a water bath at 55 °C for 3 h, during which the solution underwent a gradual color transition to orange-yellow. Thereafter, the precipitate was centrifuged, washed three times with deionized water and absolute ethanol for three times respectively, and dried in a vacuum at 60 °C for 12 h.

Synthesis of cubic Cu_2O (c-Cu_2O)

c-Cu_2O was obtained via identical experimental procedures without introducing PVP into $CuCl_2 \cdot 2H_2O$ aqueous solution.

Synthesis of 3D orthogonal cross-shaped Cu_2O (oc-Cu_2O)

Typically, oc-Cu_2O particles were fabricated as follows[2]. Initially, a homogeneous mixture was prepared by combining 2.5 mL of 2 M NaOH and 2.5 mL of 0.6 M AA

aqueous solutions, followed by dilution with 25 mL deionized water. Subsequently, the mixture was stirred for 3 h in a water bath at 55 ℃, during which the solution underwent a gradual color transition to dark-brown. Following cooling to room temperature, 36 mg of pre-synthesized t-Cu_2O samples were dispersed into the mixture under ultrasonication. Thereafter, 0.9 g of sodium citrate was introduced to the mixture. After continuous stirring for 24 h, the resultant precipitate was collected by centrifugation and washed three times with deionized water. Finally, the sample was dried under vacuum at 60 °C for 12 h.

Materials Characterizations

X-Ray Diffractometer (XRD, Smart Lab SE) with Cu Kα radiation (λ=1.5406 Å) was employed to collect the phase and structure of the materials. The X-ray photoelectron spectrometer (XPS, ESCALAB 250xi) was utilized to identify the composition of the materials. The highest peak in C 1 s spectra was shifted to 284.8 eV for charge correction. The images of the morphology of materials were collected at scanning electron microscopy (SEM, Zeiss Gemini 300 SEM). Transmission electronic microscope (TEM) and high-resolution TEM (HRTEM) images were collected using a Talos F200X G2 microscope to characterize the microstructural features.

***In-situ* characterization methods:**

***In-situ* X-ray Absorption Spectroscopy (XAS) measurements**

In-situ XAS spectra of Cu K-edge were collected at the 1W1B beamline of the Beijing Synchrotron Radiation Facility (BSRF) under electrochemical CO_2RR conditions. A custom-built *in-situ* electrochemical cell was applied using the similar configuration as a flow-cell electrolytic reacto. The catalyst ink was dispersed on a piece of gas diffusion electrode. A platinum electrode and Ag/AgCl electrode were used as the counter and reference electrode, respectively. The experiments at the 1W1B beamline were conducted in a conventional stepwise scan mode (ca. 15 min per spectrum). The XAS data was processed using the Athena and Artemis programs. All acquired X-ray absorption spectra were subjected to edge-step normalization to derive

EXAFS spectra, followed by energy calibration. The k^3-weighted $\chi(k)$ data of the Cu *K*-edge were transformed from k-space to R-space via Fourier transform (Figures S30-S33). Structural parameters in the vicinity of Cu atoms were fitted using the ARTEMIS module (Table S1).

In-situ time-resolved XAS measurements

In-situ time-resolved XAS spectra of Cu K-edge were collected at the 1W2B beamline of the Beijing Synchrotron Radiation Facility (BSRF) under electrochemical CO_2RR conditions. The material-coated ultrathin carbon paper was placed in a custom-built cell connected to a portable electrochemical workstation (CHI 1140D). All the XAS data were recorded via fluorescence modes with a Si(111) double crystal monochromator (DCM) cooled with liquid nitrogen, respectively. The experiments at the 1W2B beamline were conducted in the quick-scanning extended X-ray absorption fine-structure (QEXAFS) mode. Spectra were first collected for the material in the electrolyte solution, then after three cycles of linear sweep voltammetry (LSV), and finally under chronoamperometry (CA) conditions. To obtain high-quality spectra, the time resolution of the time-resolved XAS was set to 18 seconds.

In-situ wide-angle X-ray scattering (WAXS) measurements

The WAXS patterns were recorded using DECTRIS EIGER2 4M at the ID08-Pink Small-angle Scattering Beamline of High Energy Photon Source (HEPS-ID08). The incident X-ray energy was fixed at 12 keV (λ=1.033 Å). The data collection time for each image is 500 milliseconds. The distance from the sample to the detector was calibrated using the WAXS pattern of a LaB6 standard sample as 203 mm. In a typical measurement, the WAXS scan would go through the entire custom-built cell from the anode through an anion exchange membrane and all the way to the cathodic GDE. The 2D WAXS patterns were further converted to 1D curves using the ScatterX3 software.

In-situ Raman measurements

In-situ Raman measurements were acquired on a Jobin Yvon HR800 spectrometer equipped with a 633 nm laser, covering a spectral range of 200-2300 cm^{-1}. Raman

spectra were acquired by averaging 3 scans (10 s per scan). The measurements were carried out in a custom-built flow cell with a similar configuration as the flow cell reacto. A platinum electrode and Ag/AgCl electrode were used as the counter and reference electrode, respectively. The catalyst was applied to gas diffusion electrodes using an air-spraying technique, and the tests were performed in a 1 M KOH solution with a continuous purge of high-purity CO_2 (99.999%).

In-situ ATR-SEIRAS measurements

In-situ ATR-SEIRAS measurements were performed using a Bruker Invenio-S FT-IR spectrometer equipped with an internal reflection accessory (SPEC-I, Shanghai Yuanfang Tech. Co., Ltd., China) in a typical reactor consisting of two chambers with three electrodes. A platinum electrode and Ag/AgCl electrode were used as the counter and reference electrode, respectively. A pretreated Si face-angle crystals at an incidence angle of 60° was used as the reflection element. Au films were deposited by chemical deposition on the Si crystals[3]. The catalyst ink was deposited onto the Au film and air-dried to form the catalytic layer before testing. The electrolyte for *in-situ* ATR-SEIRAS measurements was CO_2-saturated $KHCO_3$ (0.1 M). All spectra were collected in absorbance mode with a resolution of 4 cm^{-1}, by averaging 32 scans. Infrared spectra were collected during CO_2RR while applying cathodic potentials ranging from -0.57 to -1.37 V *vs.* RHE. The electrochemical workstation (CHI 760E, Shanghai CH Instruments Co., China) was utilized for the potential control. Spectra recorded under open circuit potential (OCP) conditions were used for background subtraction. All spectra were converted to the absorbance unit as -log (I/I_0), where I and I_0 represent the signal intensities of the reflected radiation of the sample and reference spectra.

Electrochemical measurements

Preparation of GDEs

For the preparation of gas diffusion electrode (GDE), 20 mg of the catalyst powder was dispersed in a mixture of 4 mL ethanol and 80 μL 5 wt.% Nafion solution by ultrasound for 1 h. Then, the obtained ink was uniformly spray-coated onto a piece of

3 cm × 5 cm gas diffusion layer (GDL, YLS-30T) to prepare GDEs. Then, the above GDEs were heated at 60 °C for 0.5 h to remove residual ethanol, avoiding negative effects on CO_2RR performance and product analysis. The electrode with a catalyst loading density of 0.5 mg cm^{-2} was cut into 0.8 cm × 2.3 cm pieces for use.

Electrocatalytic CO_2 reduction reaction (CO_2RR) measurements

CO_2RR was conducted in a flow-cell (101017, Gaossunion, working electrode area with 0.5 cm × 2.0 cm) using electrochemical workstation (CHI 1140D). The flow-cell configuration consisted of a three-electrode system, and the as prepared GDEs, nickel foam and Ag/AgCl electrode were used as the working electrode, counter electrode and reference electrode, respectively. Electrolysis was performed in 3 M KOH, and catholyte and anolyte were separated by an anion exchange membrane (FAB-PK-130, Fuel Cell Store). The cathodic electrolyte (30 mL) was circulated through the electrolyte chambers under constant flow (5 mL min^{-1}) via peristaltic pump. The anodic electrolyte was circulated through the anodic chamber by a gas-liquid mixed flow pump. The CO_2 was supplied into gas chambers with a constant rate of 10 mL min^{-1} by a mass-flow controller, and the gas products were collected from the gas outlet and self-injected into an online gas chromatograph (GC, FULI GC9790PLUS) equipped with flame ionization detector (FID) and thermal conductivity detector (TCD) for quantitative measurements. The CO_2RR test was performed via chronoamperometry measurement with different applied potential for 1 h without IR compensation. Liquid samples were collected after 1 h electrolysis and measured by ^{1}H NMR (JEOL JNM ECZ600R 600 S2 MHz) with DMSO as an internal standard.

All potentials were converted to the reversible hydrogen electrode (RHE) according to the following equation:

$$\mathrm{E(RHE)} = \mathrm{E(Ag/AgCl)} + 0.197 + 0.0592 \times \mathrm{pH} \cdots\cdots \quad \cdots (1)$$

The Faradaic efficiency during the CO_2RR was calculated by the following equation:

$$\mathrm{FE}(\%) = \frac{e \times F \times n}{Q_{total}} \times 100\% \cdots\cdots\cdots \quad \cdots\cdots\cdots\cdots (2)$$

where e is the number of electrons transferred in the formation of certain products, F is the Faraday constant (96485 C mol^{-1}), n is the moles of certain products, and Q_{total} is the total charge consumed during CO_2RR.

The long-term stability test was operated by chronopotentiometry mode and the current density was fixed at 500 mA cm^{-2}. The electrolyte consisted of 100 mL of 3 M KOH solution, which was replaced as needed during the testing period to maintain similar ion concentrations and conductivity in the catholyte.

Electrochemical properties of different electrodes.

LSV was employed at a scan rate of 50 mV s^{-1} in 3 M KOH electrolyte under both Ar- and CO_2-fed conditions.

Electrochemical surface area (ECSA) measurements were applied by double-layer capacitance method. Non-Faradaic region (0.85 V to 0.95 V *vs.* RHE) without active peaks was selected and tested with the cyclic voltammetry (CV) method at scan rates of 20, 40, 60, 80,100 and 120 mV s^{-1}, respectively. The capacitance currents at 0.9 V vs RHE were plotted against the scan rates.

Electrochemical impedance spectroscopy (EIS) measurements were performed in a flow cell at room temperature. The EIS measurements were carried out in 3M KOH aqueous solution at different potentials, with frequencies ranging from 0.01 Hz to 100 kHz at an amplitude of 5 mV.

The OH^- adsorption reaction was carried out in an Ar-saturated 3 M KOH electrolyte using the CV at a sweep rate of 100 mV s^{-1}. The potential ranged from -0.374 to 0.626 V *vs.* RHE.

Density Functional Theory (DFT) Calculations

The first principle DFT calculations were conducted using the Vienna Ab initio Simulation Package (VASP) [4]with the projector augmented wave (PAW) [5] method. The generalized gradient approximation (GGA) was used with the Perdew-Burke-Ernzerhof (PBE) exchange-correlation functional[6]. The energy cutoff for the plane wave basis expansion was set to 400 eV. The Brillouin zone was sampled by the Gamma-centered

scheme using a 1 × 1 × 1 k-point grid. During the geometry optimization and electronic structure calculations, the convergence criterion was set to 10^{-4} eV/atom for energy and 0.05 eV/Å for the maximum force on atoms.

The slab model of Cu(100) and Cu(100)/Cu(111) surface were constructed with a vacuum layer of 15 Å, and the atoms were fully relaxed. The Gibbs free energy of reaction intermediates was evaluated using the Computational Hydrogen Electrode (CHE) method, as described by the following equation:

$$G = H - T\Delta S = E + E_{ZPE} - TS \cdots\cdots\cdots\cdots\cdots\cdots (3)$$

where E is the total energy from the DFT calculation, E_{ZPE} is the zero-point energy, S is the entropy, and T is the temperature (298 K). The free energy calculations for the molecules and intermediates during reactions were referenced to H_2, H_2O, and CH_4 molecules based on the following reactions[7]:

$$H_2 + 1/2\,O_2 \rightarrow H_2O \quad \Delta G = 0eV \cdots\cdots\cdots\cdots\cdots\cdots\cdots (4)$$

$$CH_4 + 2H_2O \rightarrow CO_2 + 4H_2 \quad \Delta G = 1.177eV \cdots\cdots\cdots\cdots\cdots\cdots (5)$$

$$CH_4 + H_2O \rightarrow CO + 3H_2 \quad \Delta G = 1.473eV \cdots\cdots\cdots\cdots\cdots\cdots (6)$$

Supplementary Figures

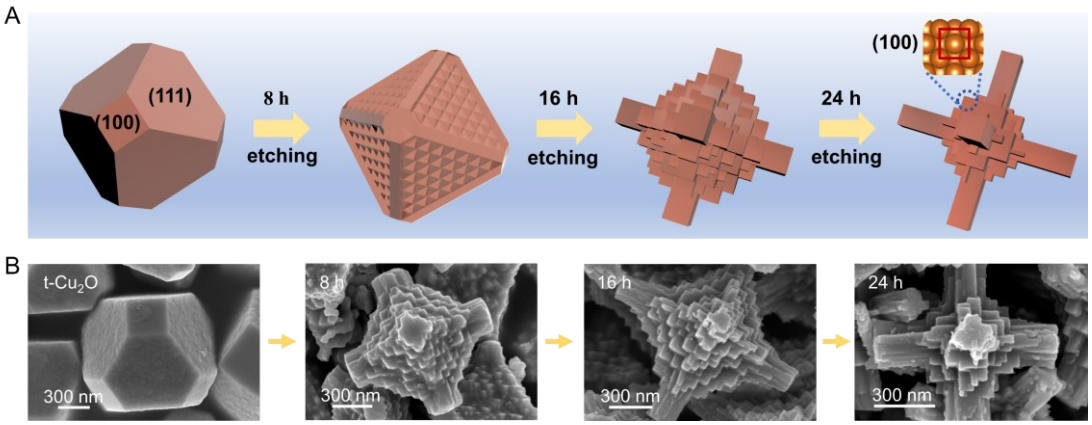

Figure S1. (A) Schematic diagrams of the synthesis of oc-Cu_2O. (B) SEM images of the materials for different etching times.

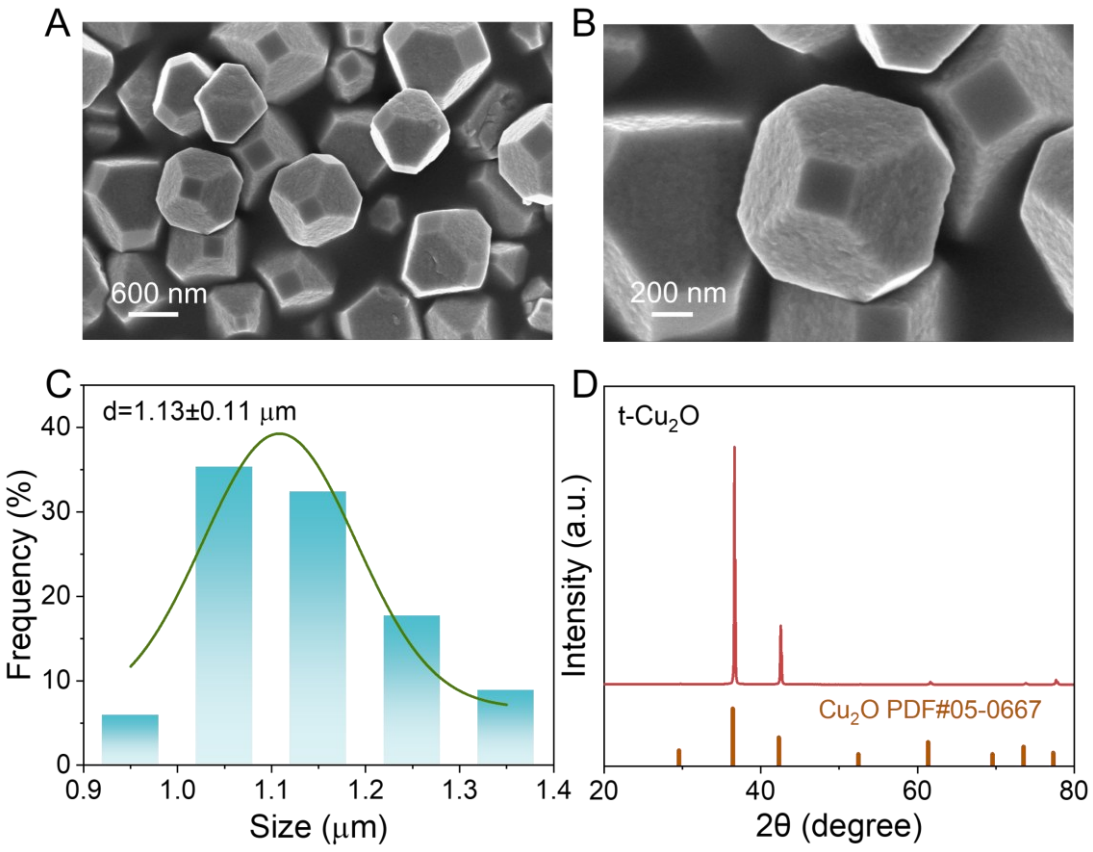

Figure S2. (A-B) SEM images, (C) particle size statistics and (D) XRD pattern of t-Cu_2O.

1 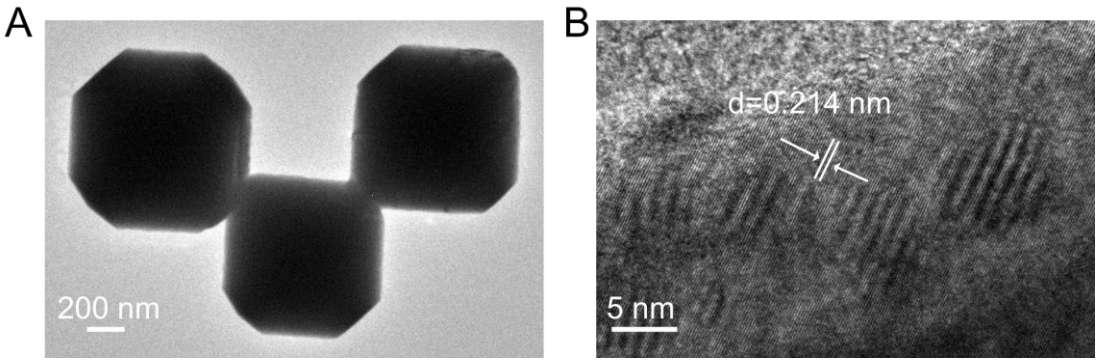

2 Figure S3. (A) TEM image and (B) HRTEM image of t-Cu_2O.

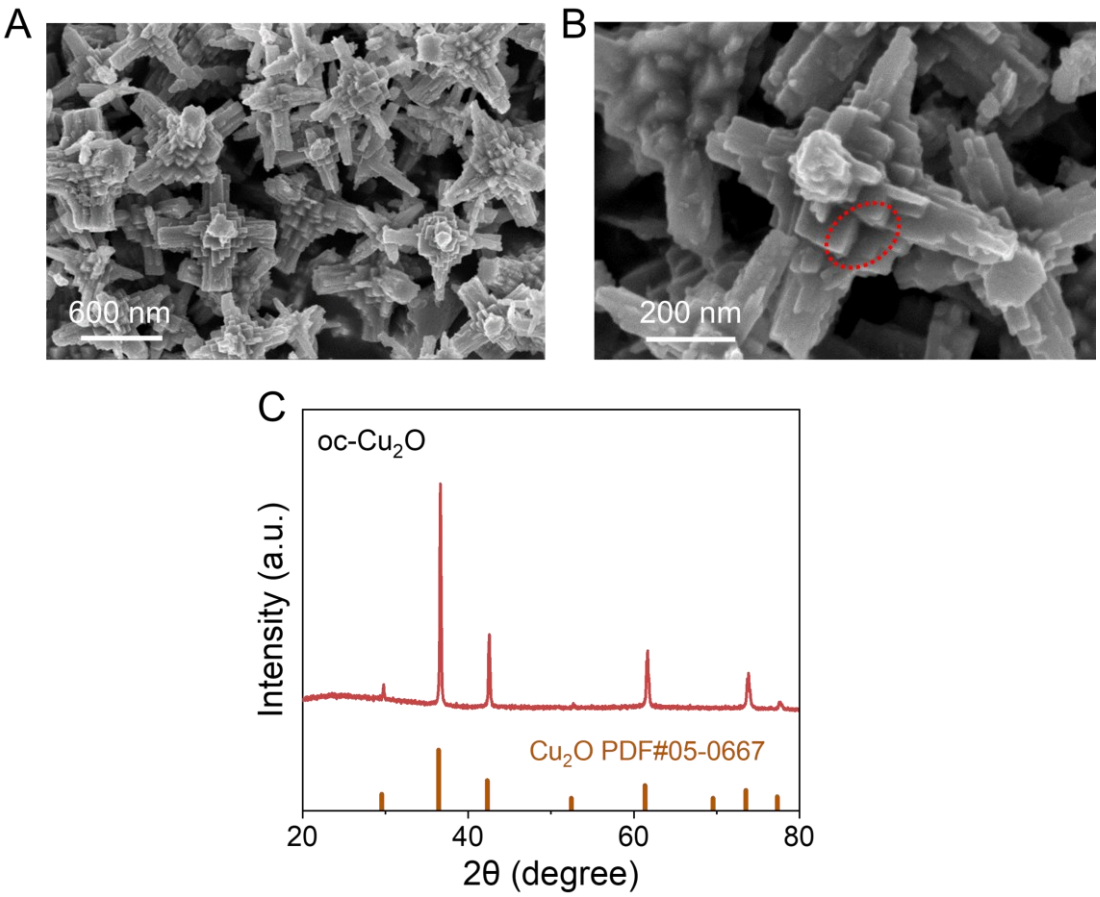

Figure S4. (A-B) SEM images and (C) XRD pattern of oc-Cu_2O.

1 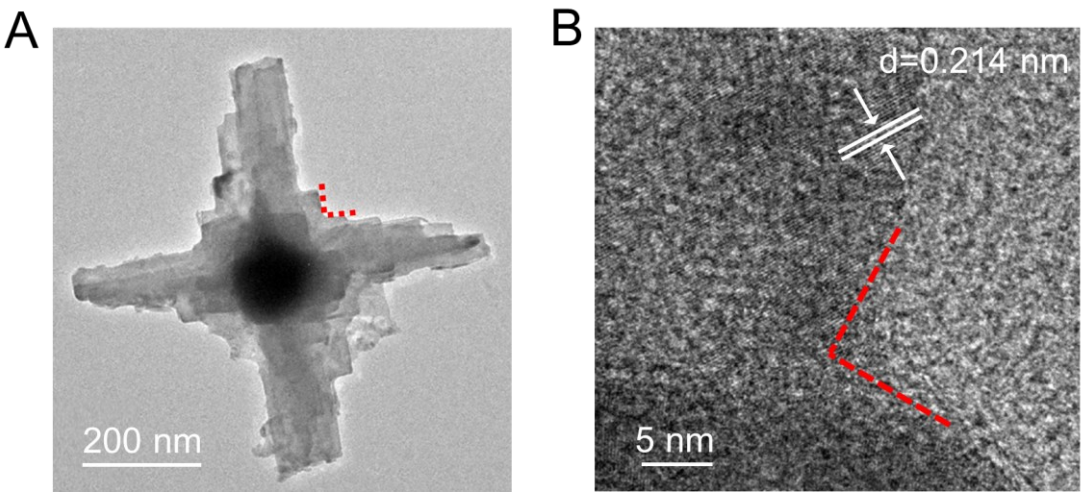

2 Figure S5. (A) TEM image and (B) HRTEM image of oc-Cu_2O.

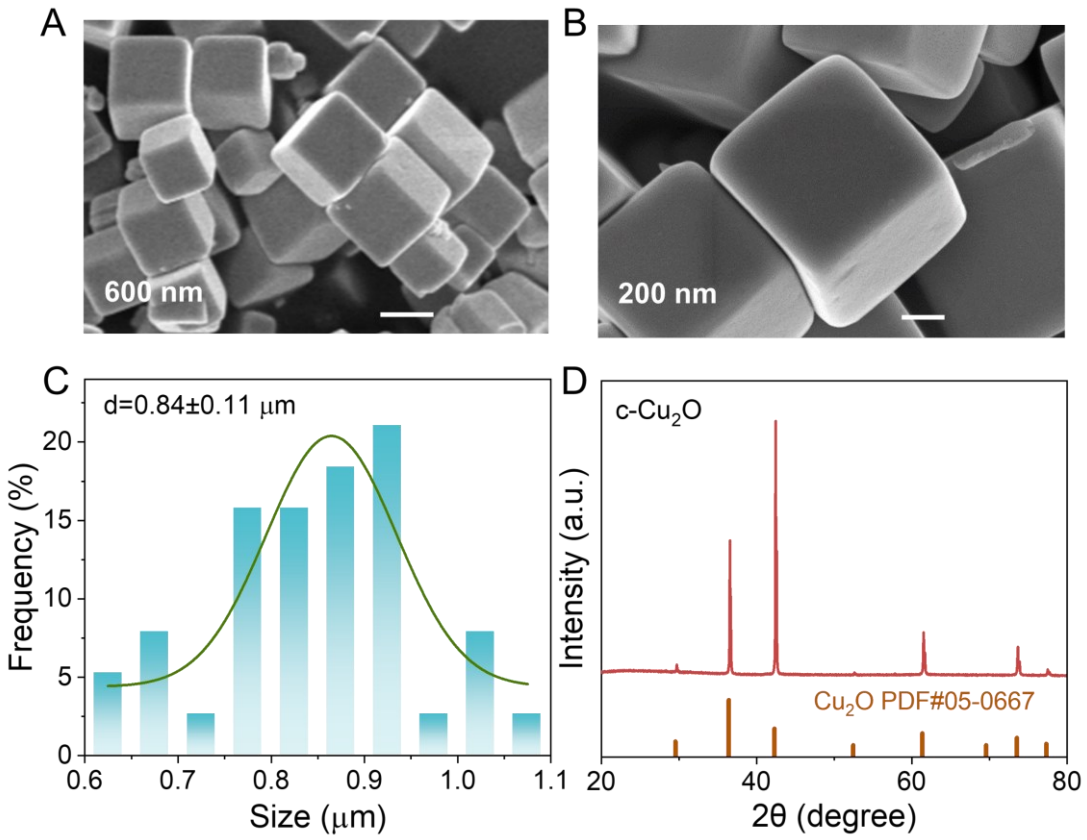

Figure S6. (A-B) SEM images, (C) particle size statistics and (D) XRD pattern of c-Cu_2O.

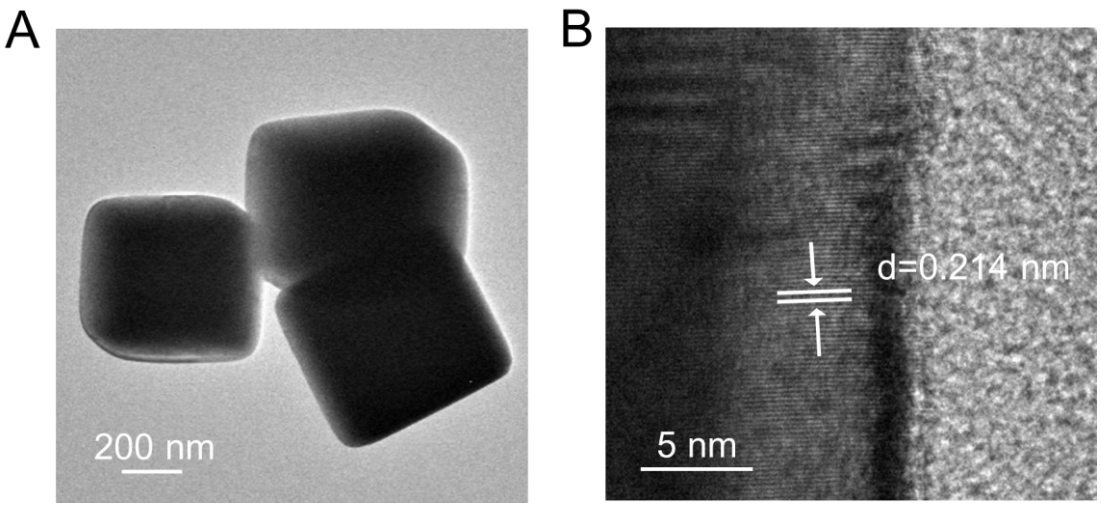

Figure S7. (A) TEM image and (B) HRTEM image of c-Cu_2O.

1 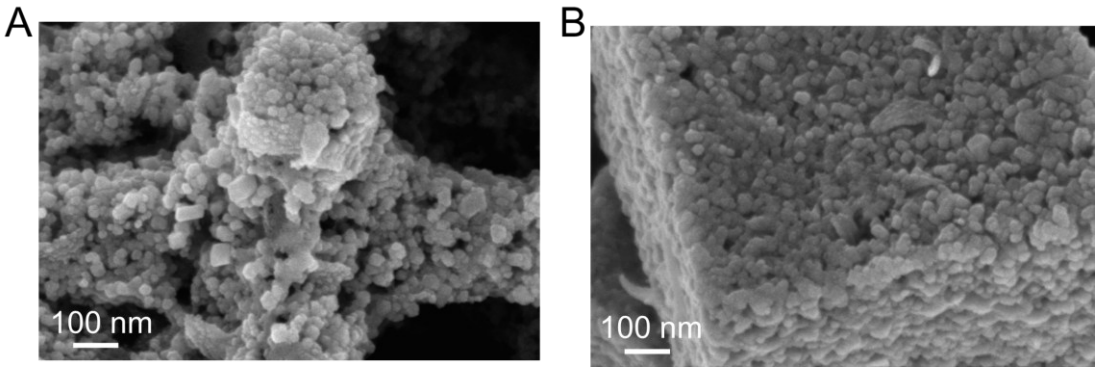

2 Figure S8. SEM images of the materials after LSV treatment. (A) oc-Cu_2O. (B) c-Cu_2O.

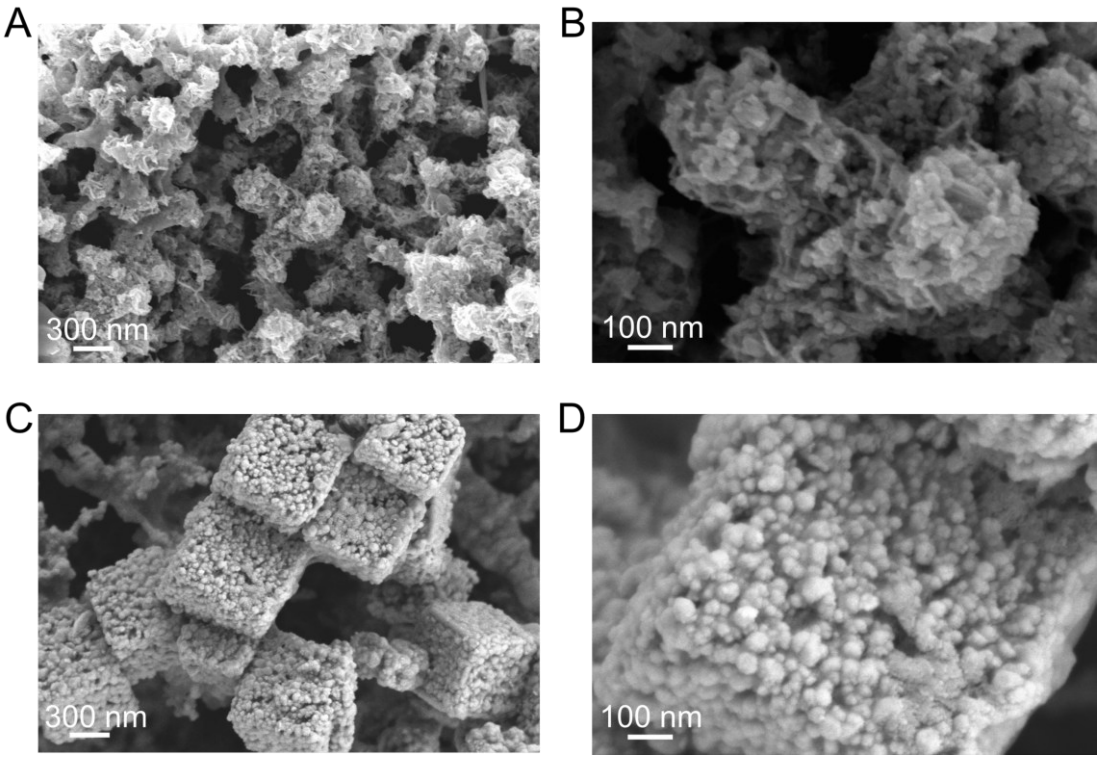

Figure S9. SEM images of the materials after CA treatment for 8 min. (A-B) oc-Cu_2O. (C-B) c-Cu_2O.

1 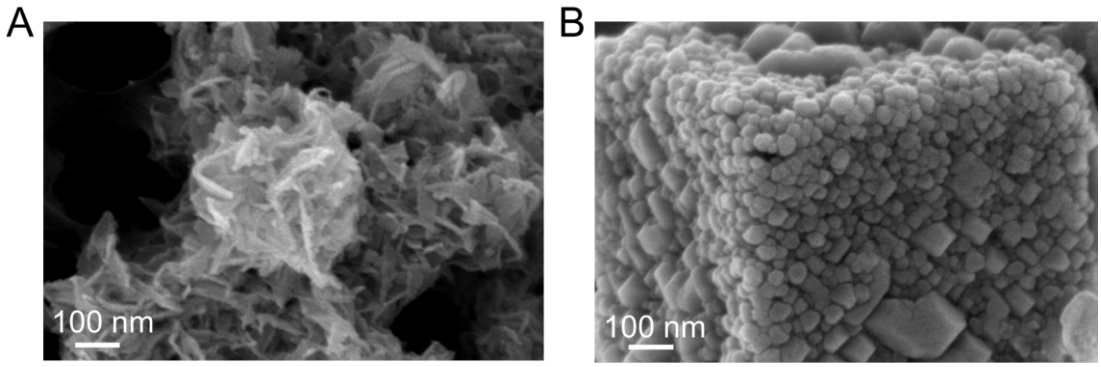

2 Figure S10. SEM images of the materials after CA treatment for 15 min. (A) oc-Cu_2O.

3 (B) c-Cu_2O.

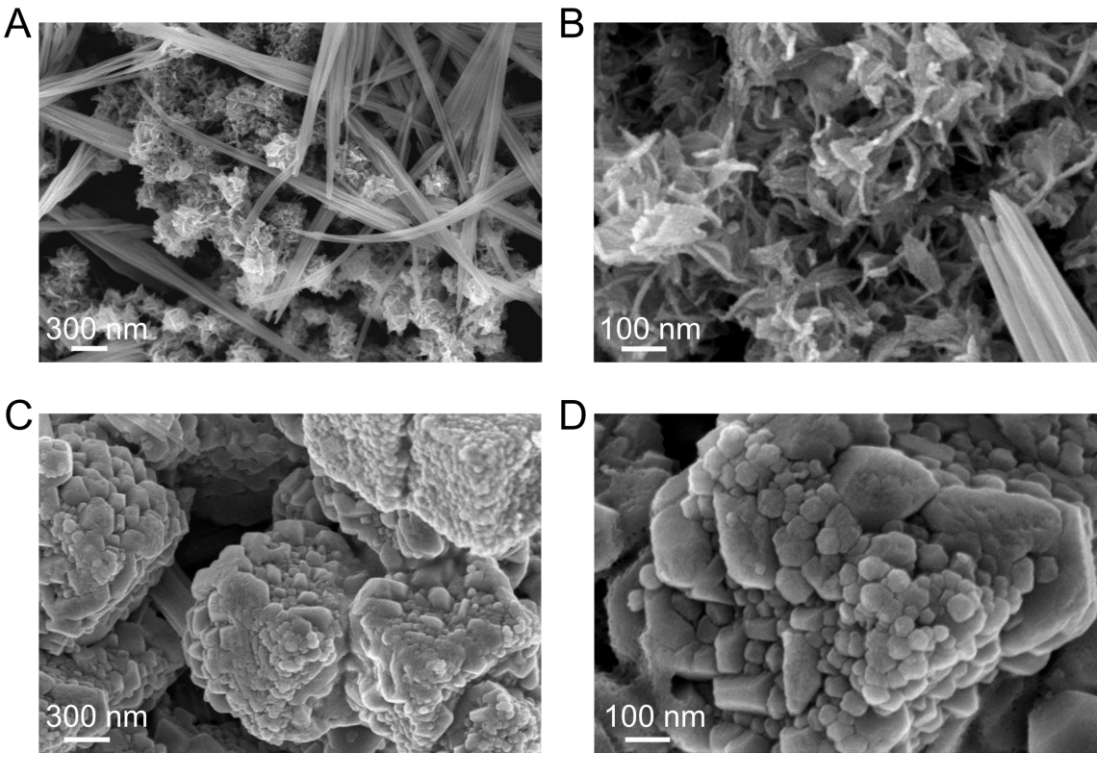

Figure S11. SEM images of the materials after CA treatment for 23 min. (A-B) oc-Cu_2O. (C-B) c-Cu_2O.

1 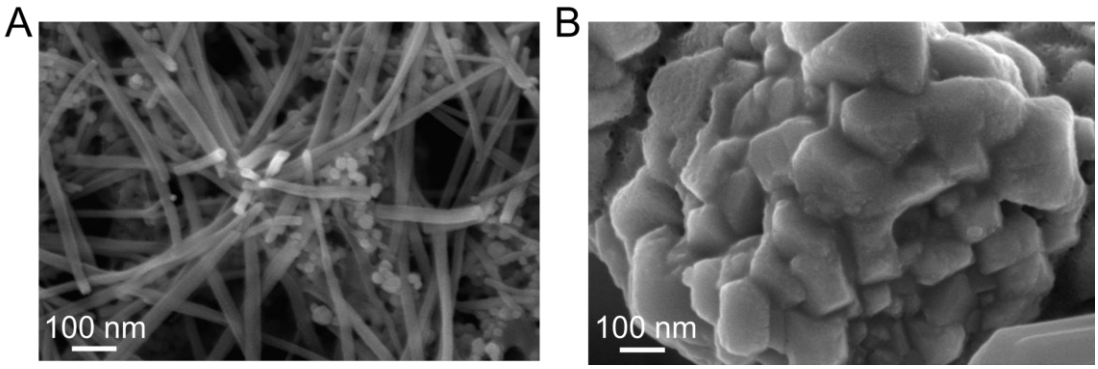

2 Figure S12. SEM images of the materials s after CA treatment for 30 min. (A) oc-Cu_2O.

3 (B) c-Cu_2O.

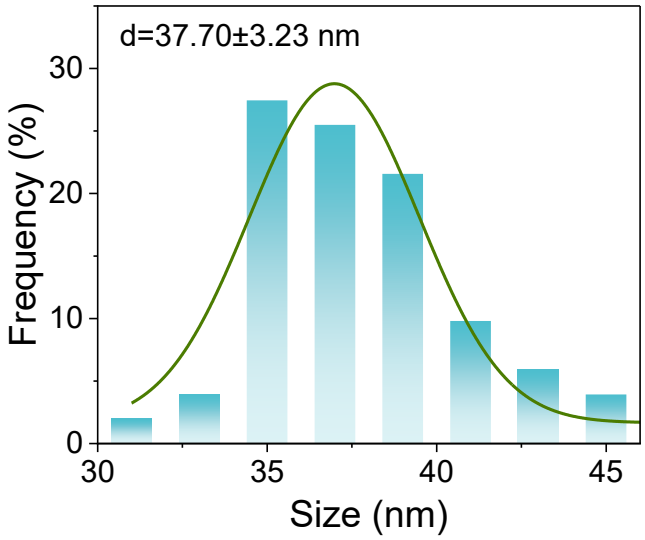

Figure S13. Particle size statistics of NR-Cu.

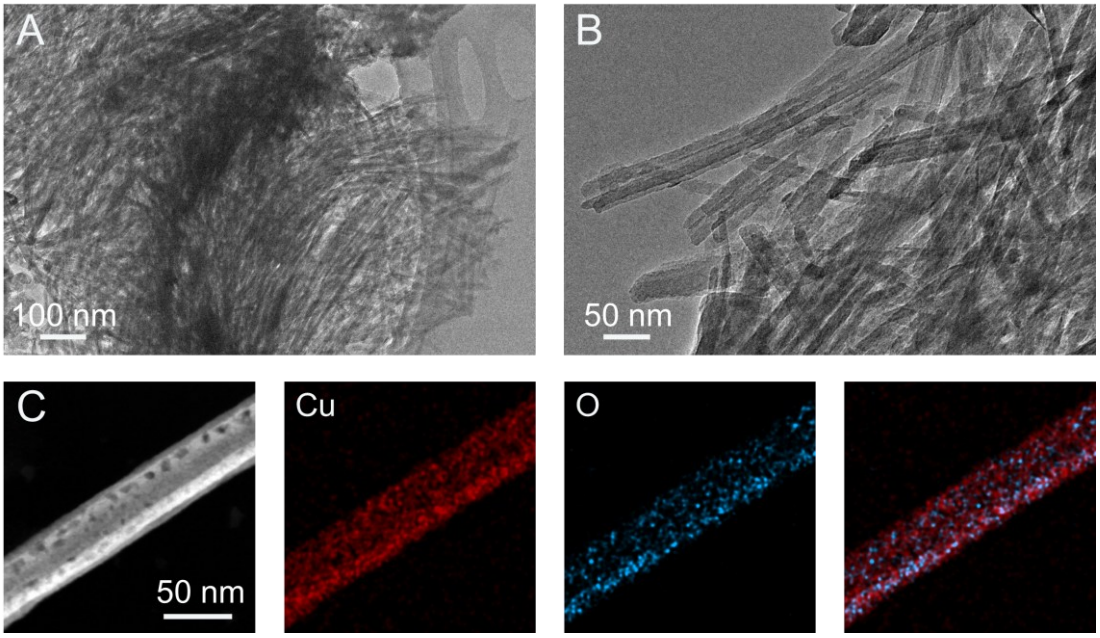

Figure S14. (A-B) TEM images of NR-Cu and (C) corresponding EDS elemental mapping images.

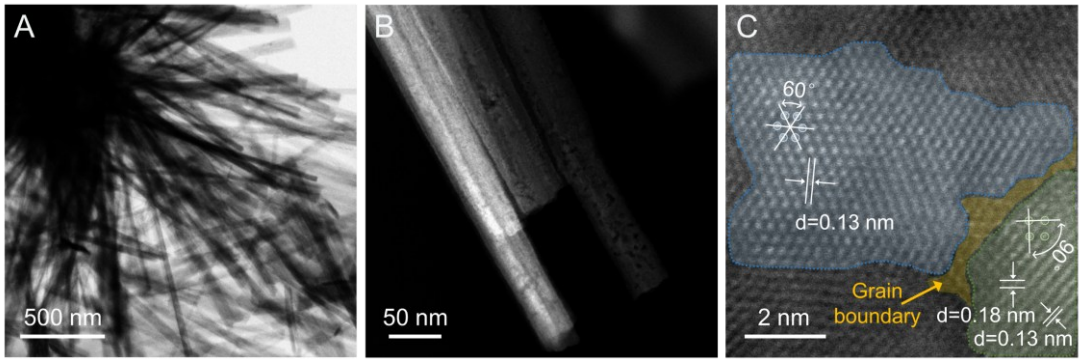

Figure S15. (A-B) HAADF-STEM image and (C) atomically resolved HAADF-STEM images of NR-Cu. The region outlined in blue, green and yellow represent Cu(111) fact, Cu(100) fact and disordered grain boundary, respectively.

1 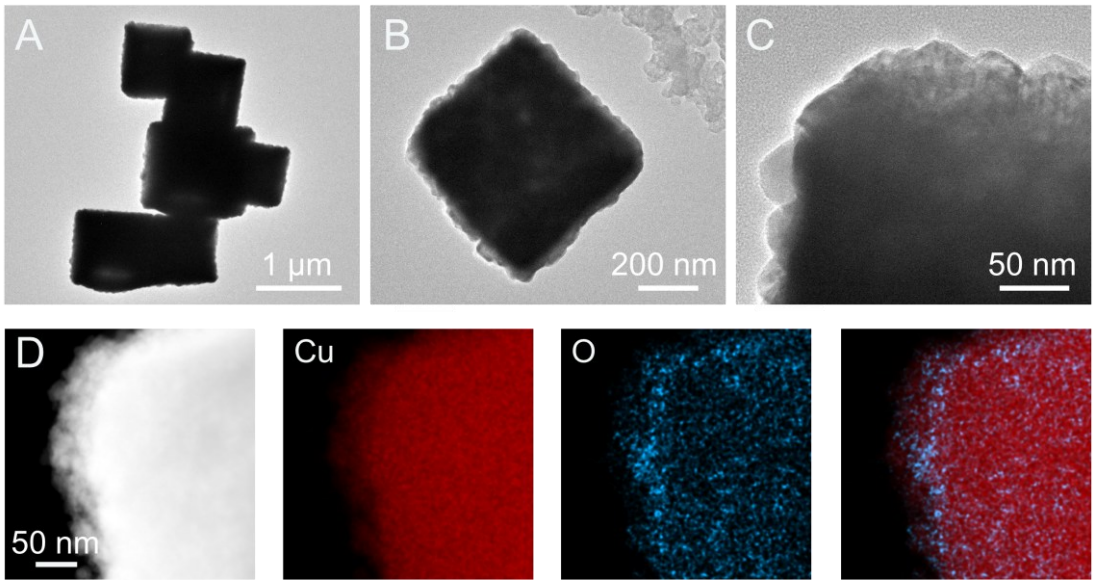

2 Figure S16. (A-C) TEM images and (D) corresponding EDS elemental mapping
3 images of C-Cu.

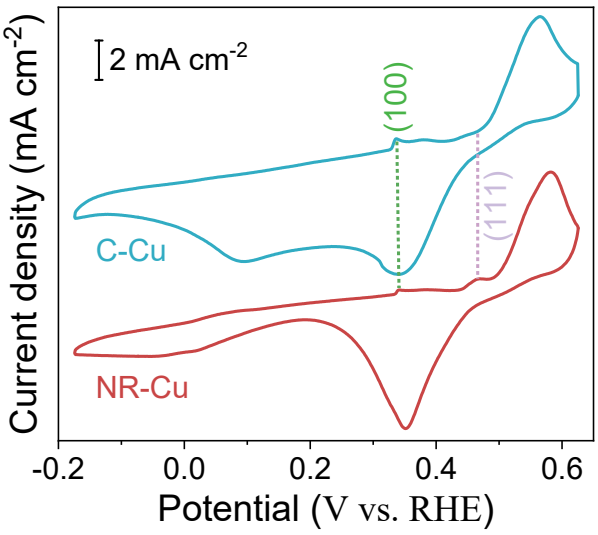

Figure S17. OH^- electroadsorption profiles. CV curves of NR-Cu (red) and C-Cu (blue) in Ar-saturated 3 M KOH, Scan rate = 100 mV s^{-1}. Different Cu facets exhibit unique OH-adsorption/desorption peaks in the CV curves. The peaks centered at ca. 0.35 and 0.46 V *vs.* RHE can be assigned to the OH-electrosorption on Cu(100) and Cu(111), respectively[8].

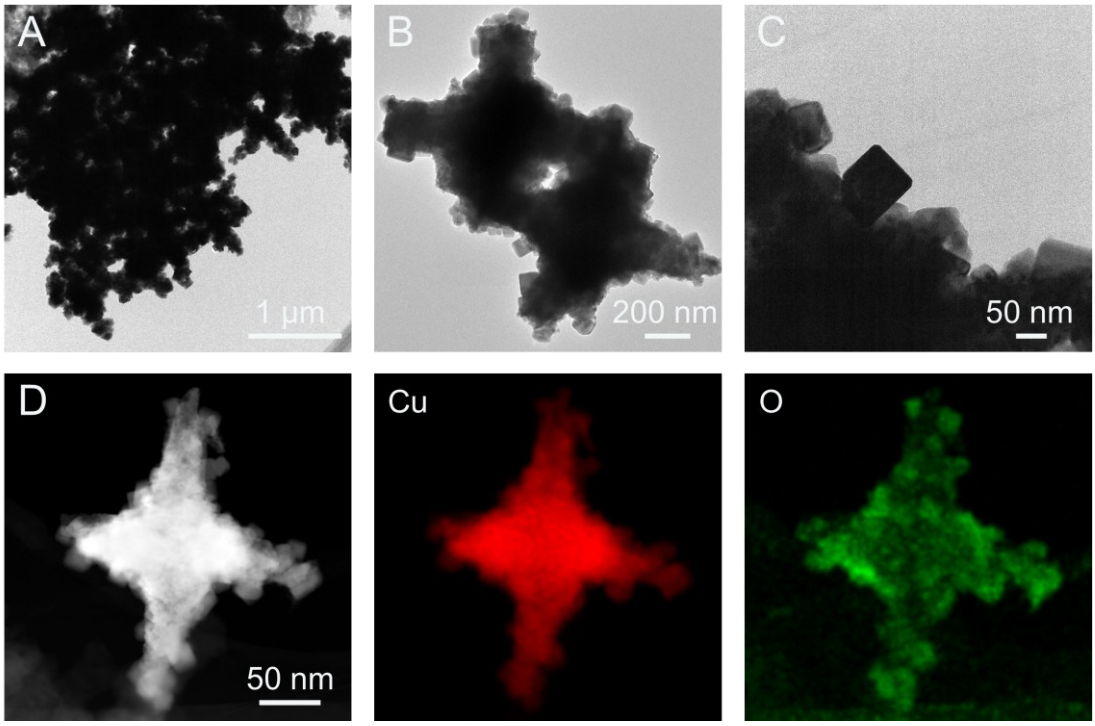

Figure S18. (A-C) TEM images and (D) corresponding EDS elemental mapping images of OC-Cu.

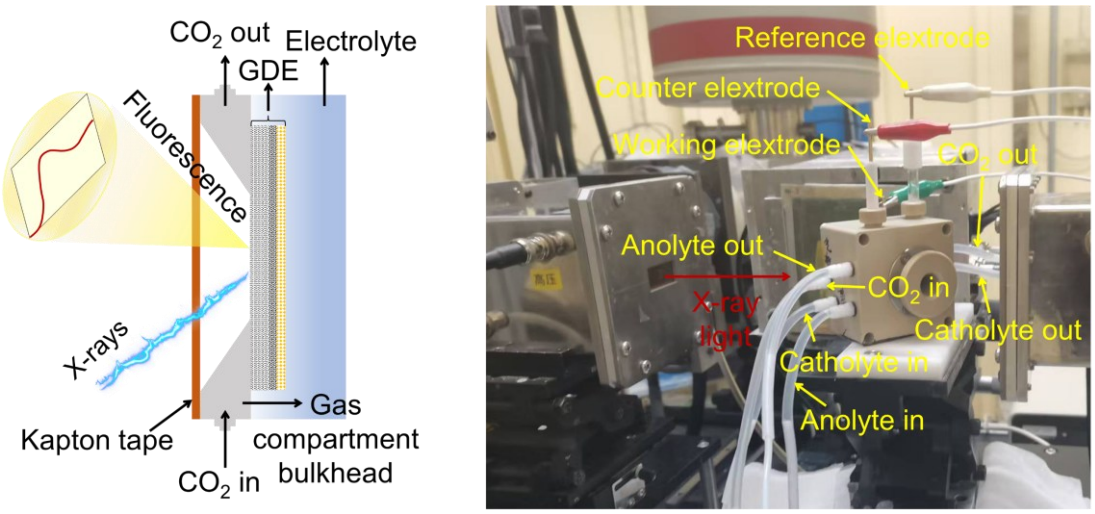

1

2 Figure S19. Schematic diagram (left) and photograph (right) of the *in-situ* XAS

3 experimental setup.

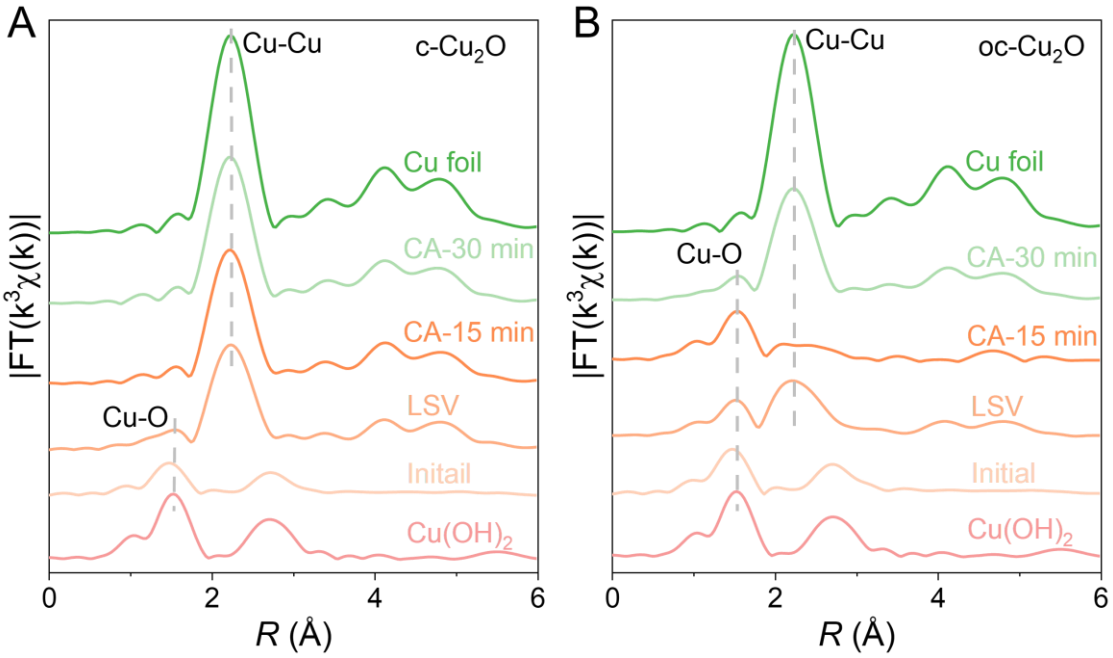

Figure S20. EXAFS spectra of (A) c-Cu_2O and (B) oc-Cu_2O at different treatment times.

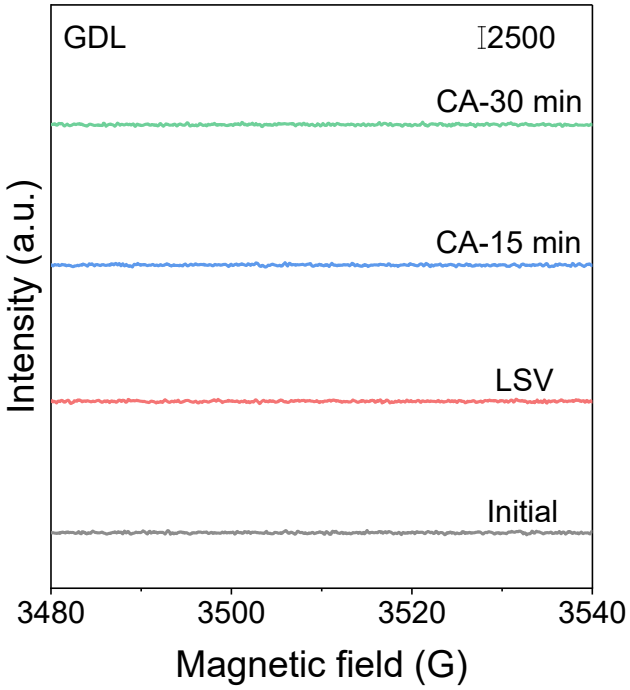

Figure S21. *In-situ* EPR spectra of GDL (without catalytic material) in 3 M KOH electrolyte at different treatment times. No characteristic •OH electron paramagnetic resonance signals were detected for the GDL (without catalytic material) during LSV activation and CA treatment. The results excluded the possibility that the KOH electrolyte itself generated strongly oxidative radicals.

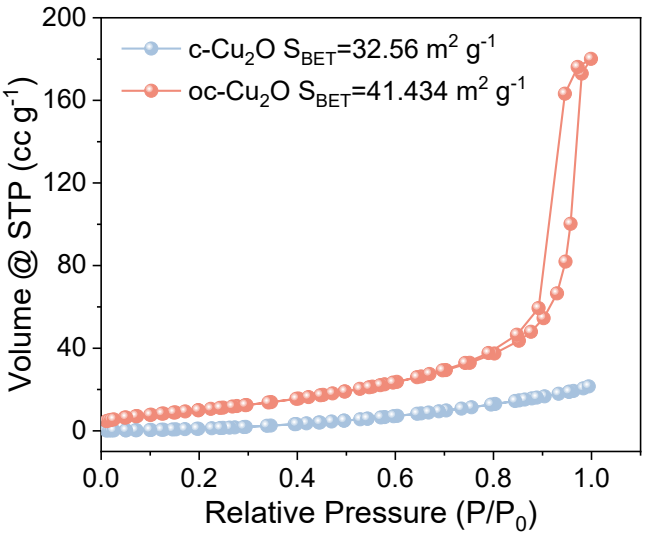

Figure S22. Nitrogen adsorption-desorption isotherms of oc-Cu_2O (red) and c-Cu_2O (blue).

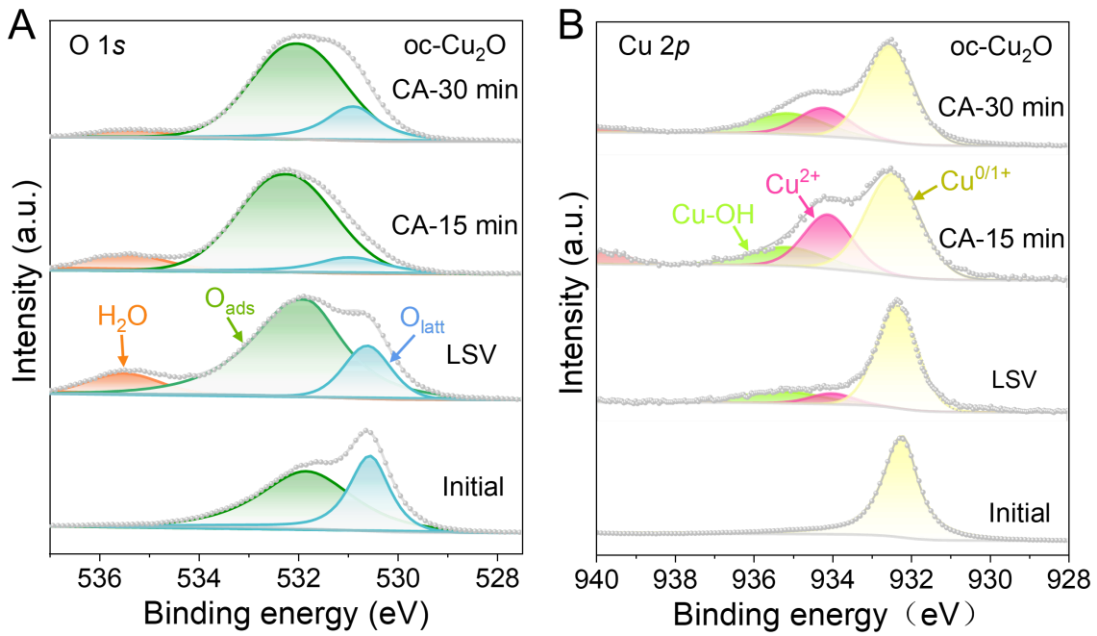

Figure S23. (A) O 1*s* and (B) Cu 2*p* spectra for oc-Cu_2O at different treatment times.

The O 1*s* spectrum of oc-Cu_2O displayed characteristic peaks corresponding to adsorbed oxygen (O_{ads}, ~532.4 eV) and O_{latt} (~530.6 eV) [9,10]. LSV activation drastically increased the O_{ads} signal, which became dominant, likely attributable to the conversion of O_{latt} into surface-adsorbed •OH after accepting electrons[10,11]. Upon extending CA to 15 minutes for LSV-pretreated oc-Cu_2O, the O_{latt} signal further dropped while O_{ads} grew. The corresponding Cu 2*p* spectrum developed features of Cu-OH (~935.2 eV) and intensified Cu^{2+} signatures (~934.1 eV), suggesting •OH-mediated oxidation of Cu[10-12]. After prolonging CA treatment to 30 minutes, the Cu 2p spectra showed a decrease in the characteristic peaks corresponding to Cu-OH and Cu^{2+} species, indicating the electroreduction of the oxidized Cu species.

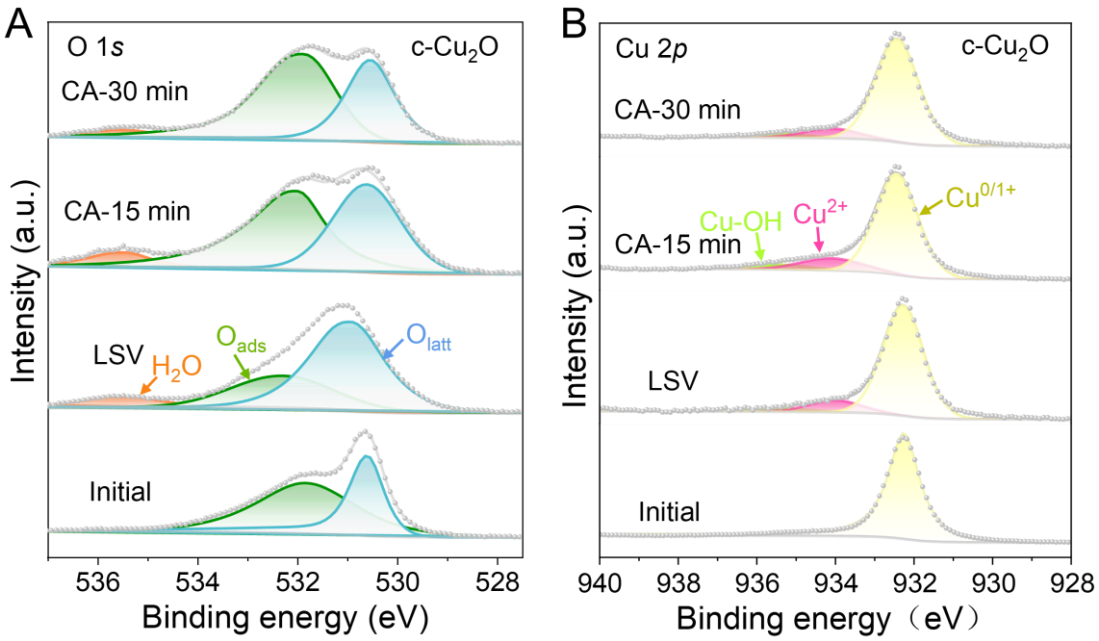

Figure S24. (A) O 1*s* and (B) Cu 2*p* spectra for c-Cu_2O at different treatment times. The O 1*s* spectrum of c-Cu_2O displayed characteristic peaks corresponding to adsorbed oxygen (O_{ads}, ~532 eV) and O_{latt} (~530.6 eV). The Cu 2*p* spectrum of c-Cu_2O displayed characteristic peaks corresponding to Cu^{2+} signatures (~934.1 eV) and Cu-OH (~935.2 eV). Compared to oc-Cu_2O, c-Cu_2O exhibited relatively slower O_{ads} growth and less Cu-OH formation during LSV activation and CA treatmen. Thus, possibly constrained by its cubic structure, c-Cu_2O converts a relatively lower proportion of its O_{latt} into •OH species.

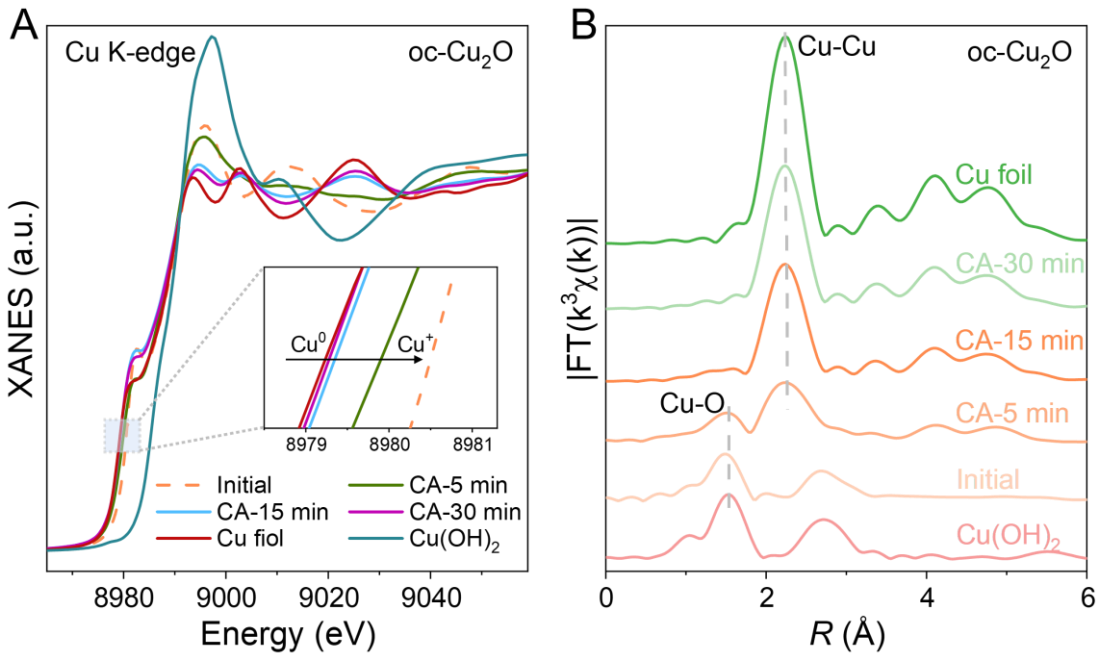

1

2 Figure S25. (A) Cu K-edge XANES and (B) EXAFS spectra for oc-Cu_2O under 30-min

3 CA treatment (without LSV).

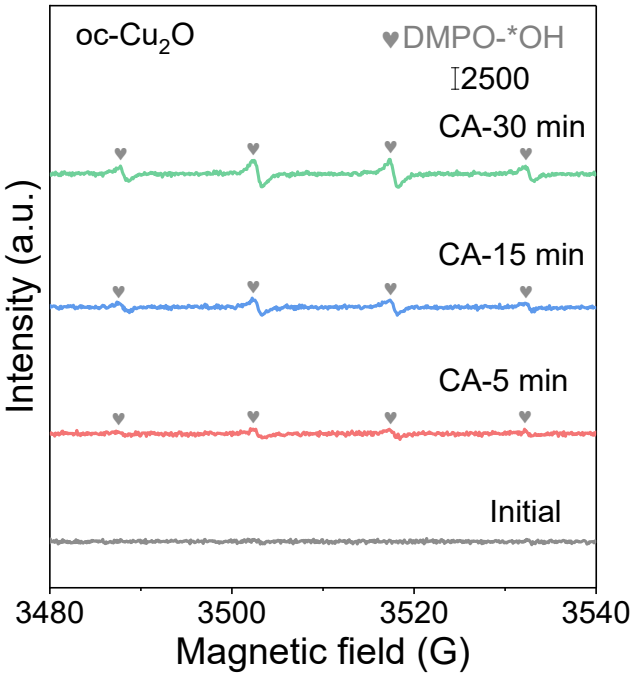

Figure S26. *In-situ* EPR spectra of oc-Cu_2O during 30-min CA treatment (without LSV) in 3 M KOH electrolyte.

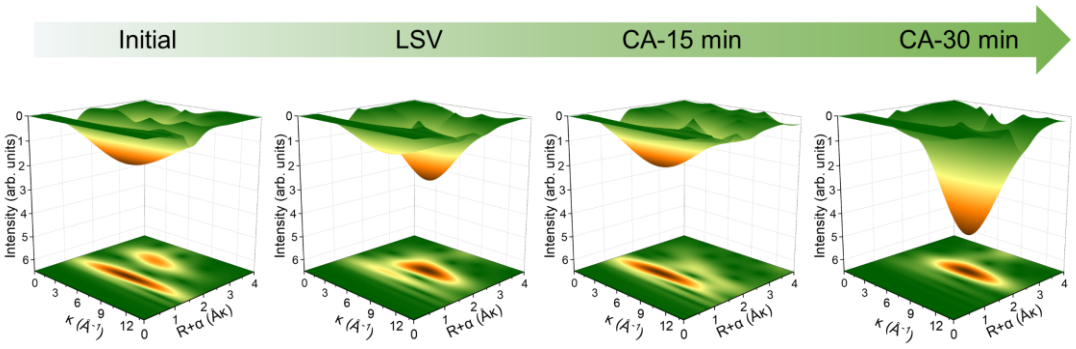

Figure S27. Contour plots of the Morlet wavelet transform tracking the reduction of oc-Cu_2O to NR-Cu over time.

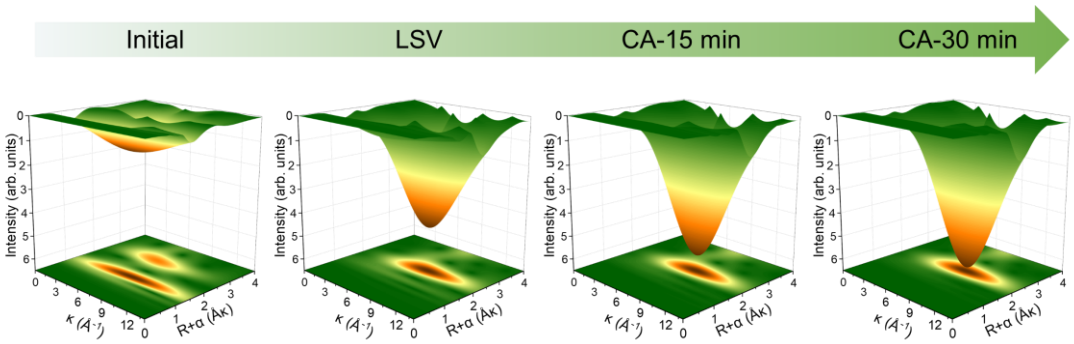

Figure S28. Contour plots of the Morlet wavelet transform tracking the reduction of c-Cu_2O to C-Cu over time.

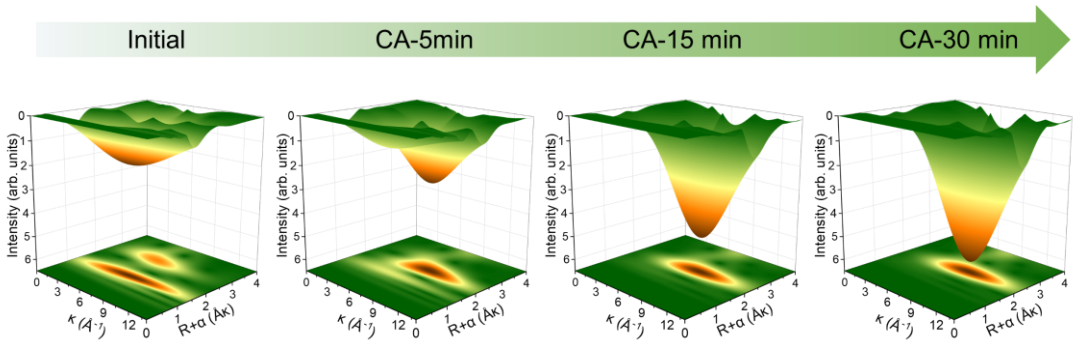

Figure S29. Contour plots of the Morlet wavelet transform tracking the reduction of oc-Cu_2O to OC-Cu over time.

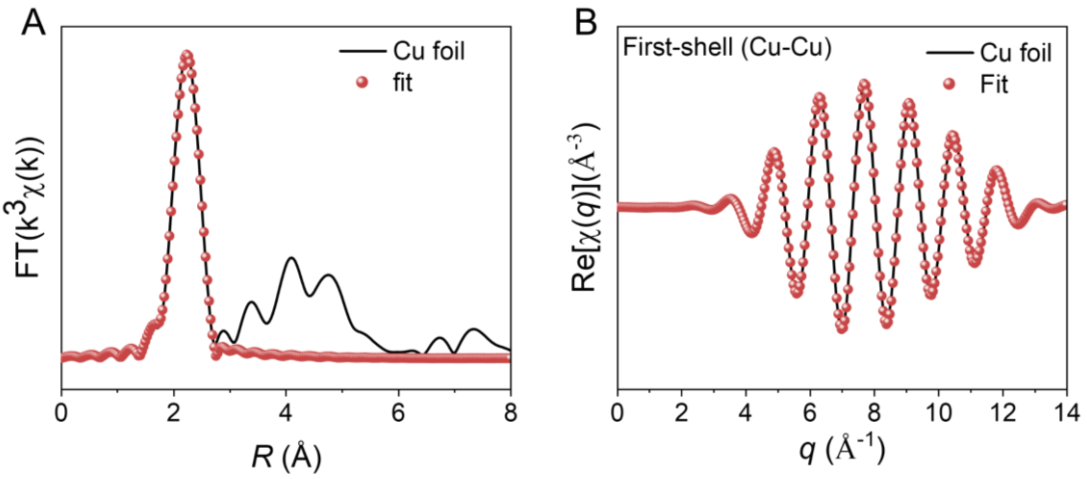

Figure S30. (A) Cu K-edge EXAFS fitting curves of Cu foil in R space. (B) The back ward FT and the corresponding fitting curves for the first shell (Cu-Cu).

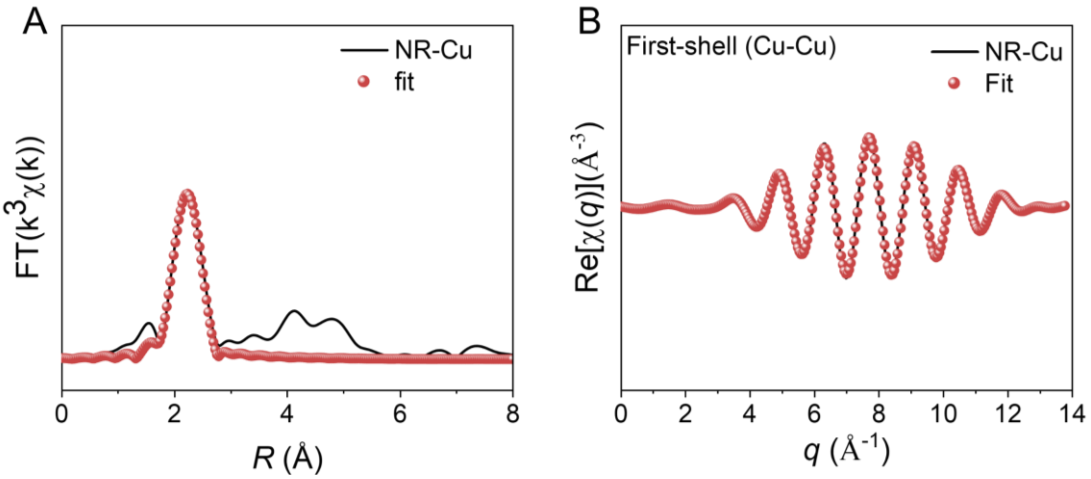

Figure S31. (A) Cu K-edge EXAFS fitting curves of NR-Cu in R space. (B) The back ward FT and the corresponding fitting curves for the first shell (Cu-Cu).

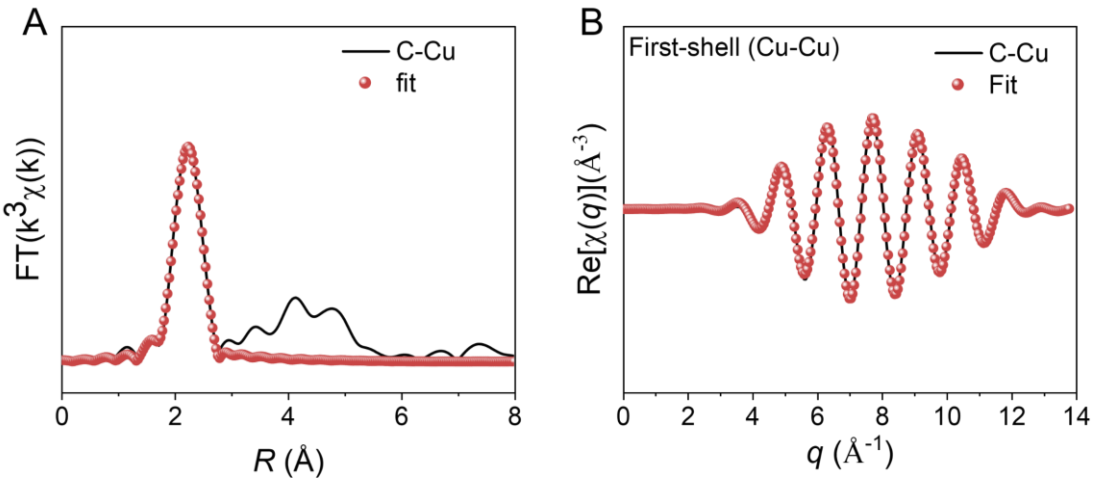

Figure S32. (A) Cu K-edge EXAFS fitting curves of C-Cu in R space. (B) The back ward FT and the corresponding fitting curves for the first shell (Cu-Cu).

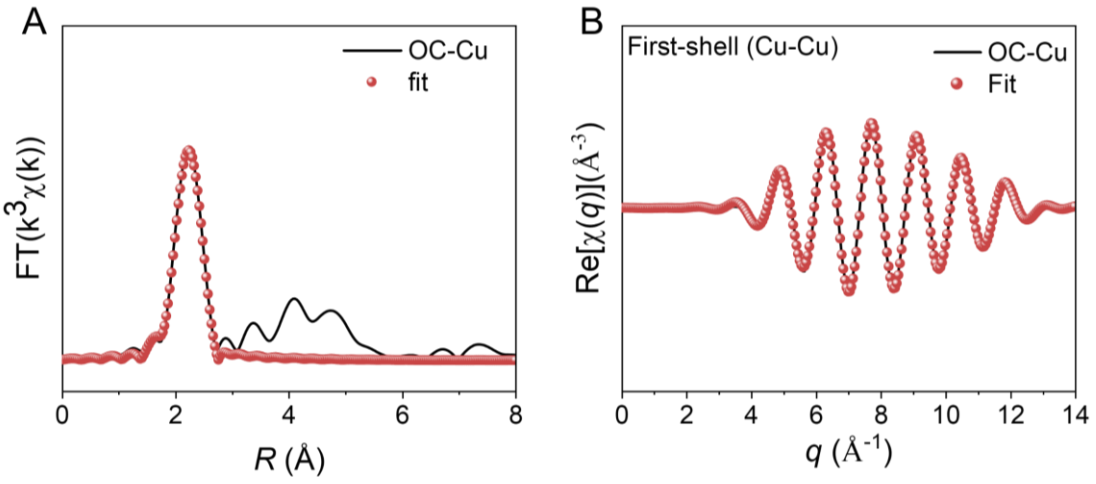

Figure S33. (A) Cu K-edge EXAFS fitting curves of OC-Cu in R space. (B) The back ward FT and the corresponding fitting curves for the first shell (Cu-Cu).

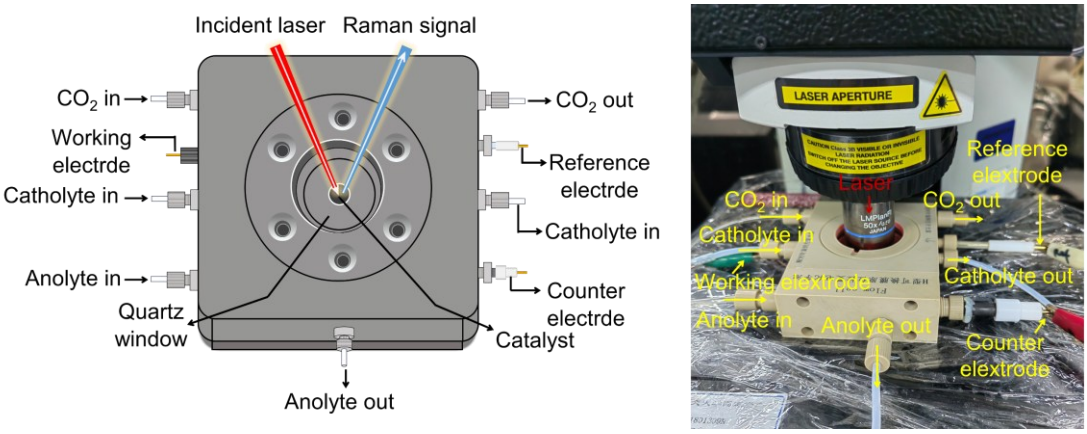

Figure S34. Schematic diagram (left) and photograph (right) of the *in-situ* electrochemical Raman setup.

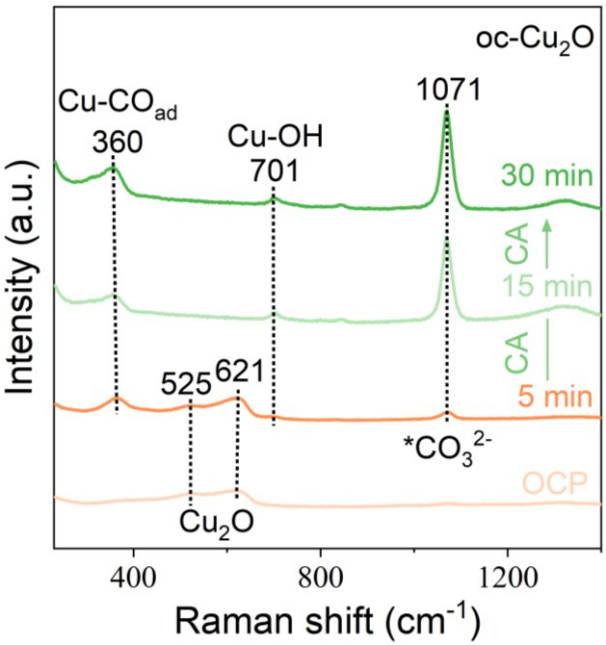

Figure S35. *In-situ* Raman spectra of oc-Cu_2O under 30-min CA treatment (without LSV).

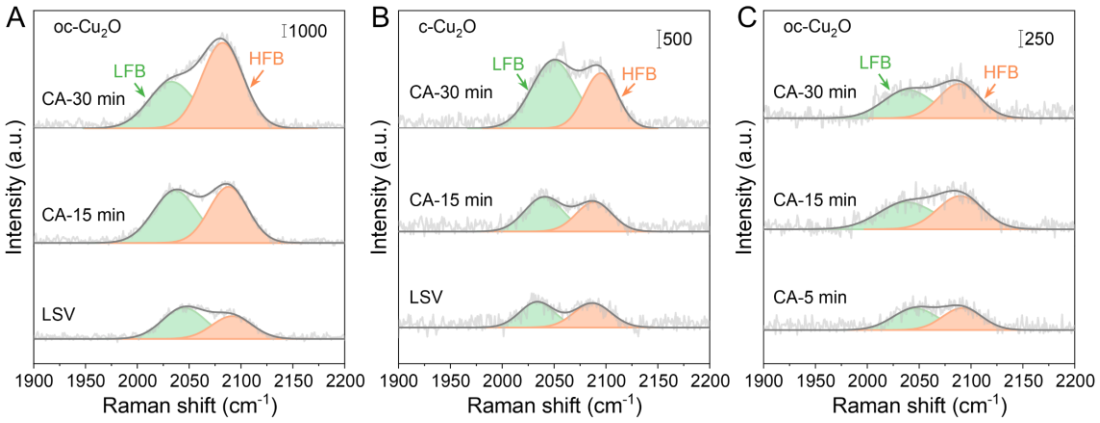

Figure S36. *In-situ* spectra analysis in the range of 1900-2200 cm^{-1}. (A) oc-Cu_2O during LSV activation and subsequent 30 min CA treatment. (B) c-Cu_2O during LSV activation and subsequent 30 min CA treatment. (C) oc-Cu_2O during 30 min CA treatment without prior LSV activation.

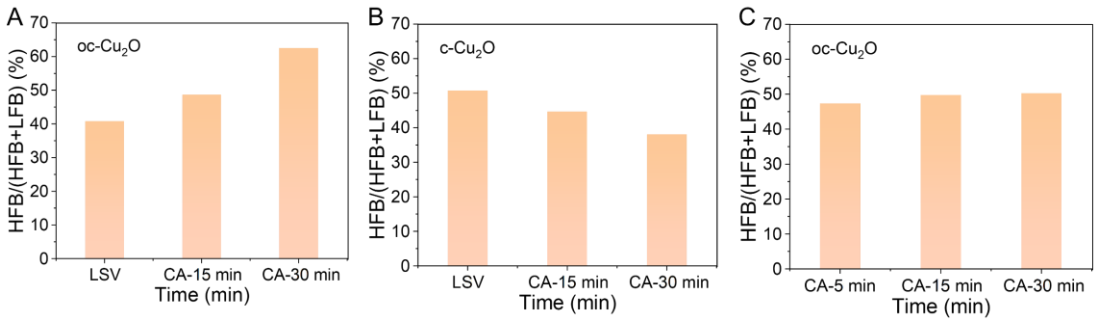

Figure S37. Comparison of the HFB/(HFB+LFB) ratio tracking the reconstruction process of different Cu_2O samples over time. (A) oc-Cu_2O to NR-Cu. (B) c-Cu_2O to C-Cu. (C) oc-Cu_2O to OC-Cu.

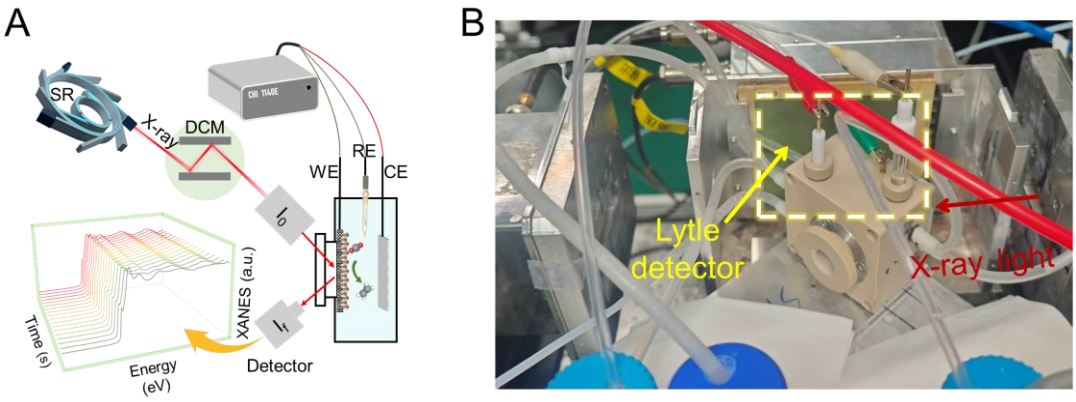

Figure S38. Schematic diagram (left) and photograph (right) of the *in-situ* time-resolved XAS measurement setup.

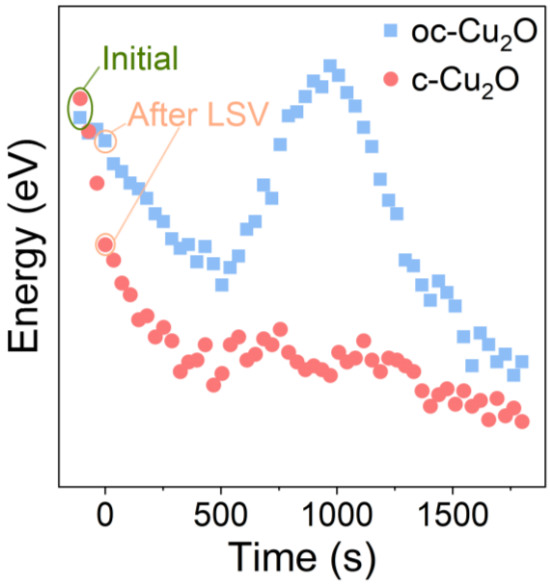

Figure S39. The Cu K-edge positions ($F/I_0 = 0.3$) of oc-Cu_2O and c-Cu_2O against the reconstruction reaction time. For oc-Cu_2O, the Cu K-edge position ($F/I_0 = 0.3$) shifted to lower energy at the initial stage of the reaction, then reversed to a higher energy direction in the middle stage (exceeding the initial position), and finally shifted back to lower energy in the late stage. This evolution pattern involves three distinct stages, reflecting a broad valence oscillation. For c-Cu_2O, the Cu K-edge position ($F/I_0 = 0.3$) shifted to lower energy as a function of reaction time, reaching its minimum value upon completion of the reconstruction. This evolution pattern exhibits a monotonic reduction characteristic, with no broad valence oscillation involved.

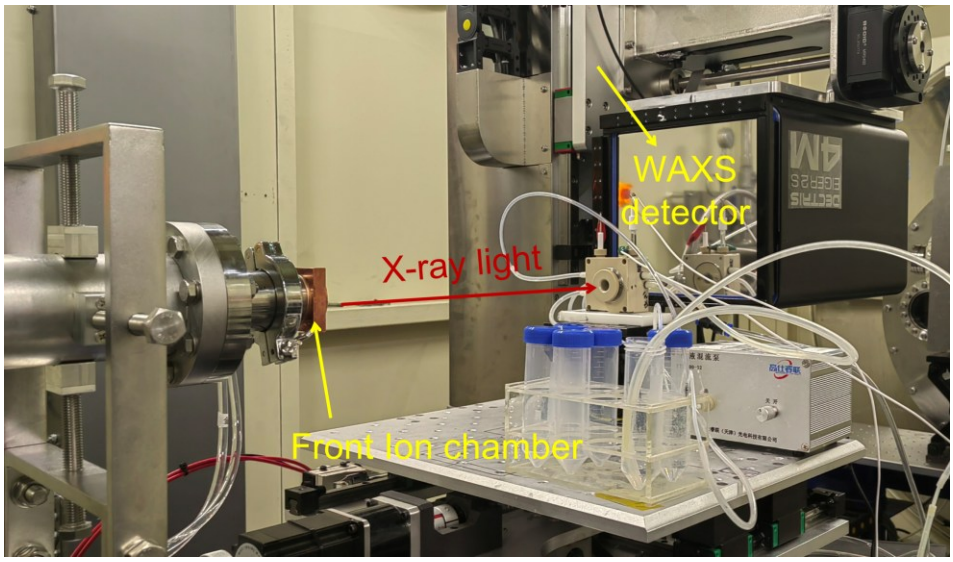

Figure S40. Photograph of the *in-situ* WAXS setup.

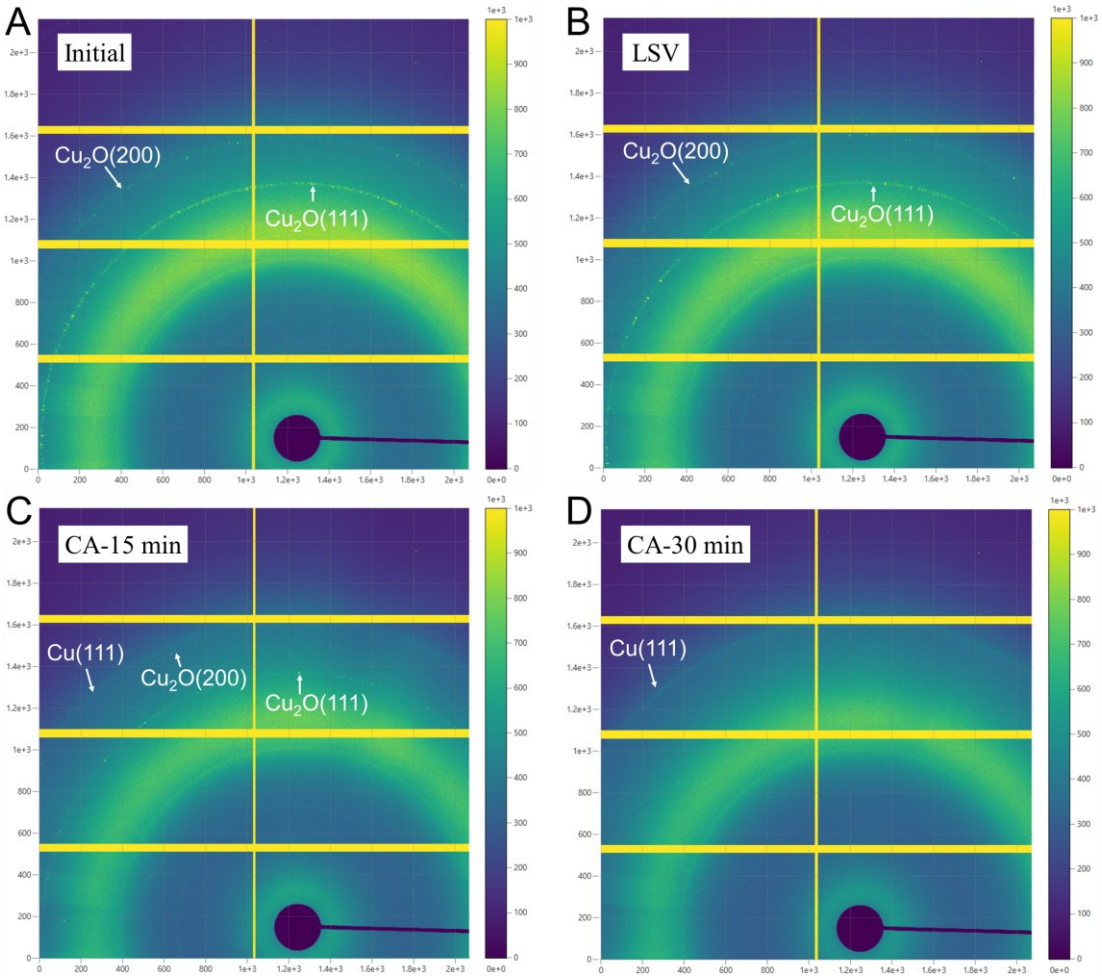

Figure S41. 2D WAXS patterns of oc-Cu_2O at different treatment times. (A) Initial. (B) After LSV activations. (C) After CA treatment for 15 min. (D) After CA treatment for 30 min. All scattering rings in the WAXS pattern can be indexed to their characteristic crystalline phases. According to the curves of scattering intensity as a function of the diffraction angle (2θ), the diffraction rings are assigned to $Cu_2O(111)$, $Cu_2O(200)$, and Cu(111), respectively.

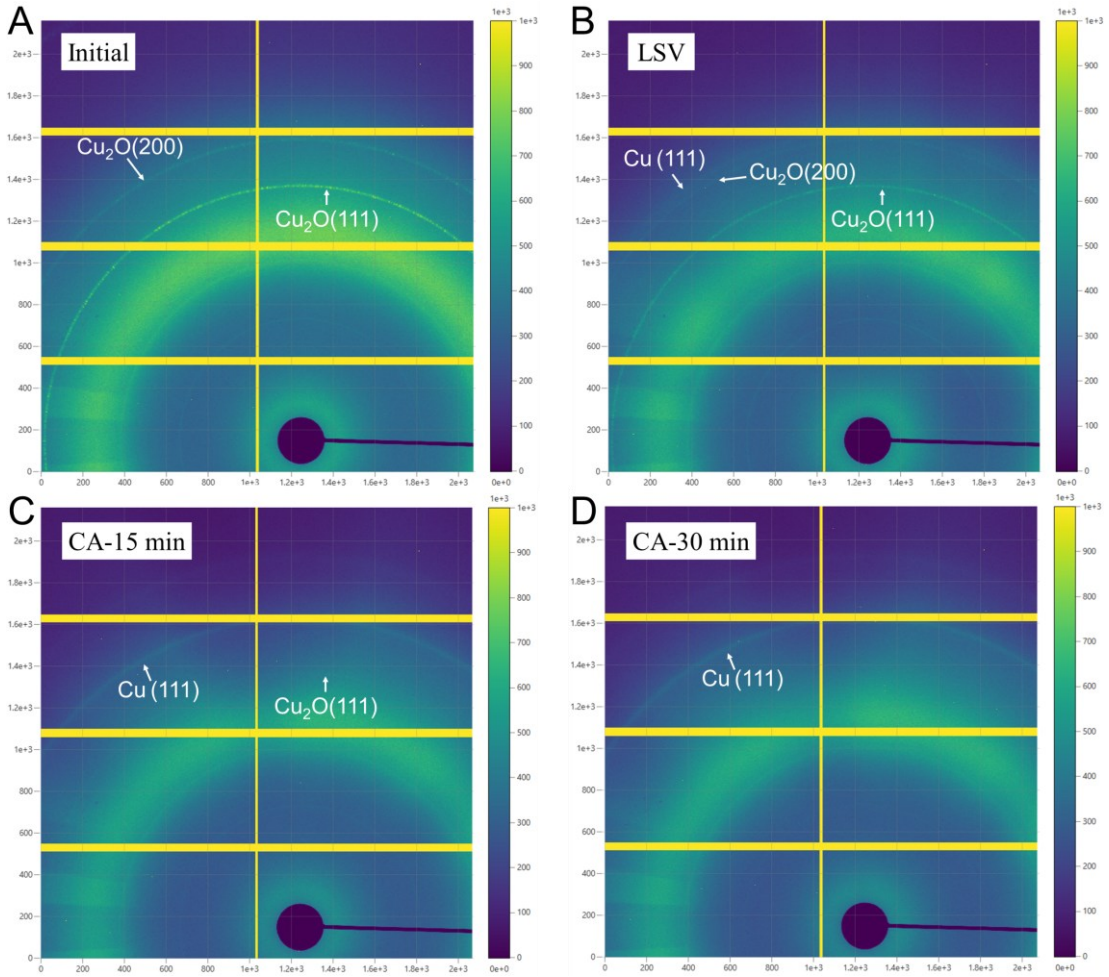

Figure S42. 2D WAXS patterns of c-Cu_2O at different treatment times. (A) Initial. (B) After LSV activations. (C) After CA treatment for 15 min. (D) After CA treatment for 30 min. All scattering rings in the WAXS pattern can be indexed to their characteristic crystalline phases. According to the curves of scattering intensity as a function of the diffraction angle (2θ), the diffraction rings are assigned to Cu_2O(111), Cu_2O(200), and Cu(111), respectively.

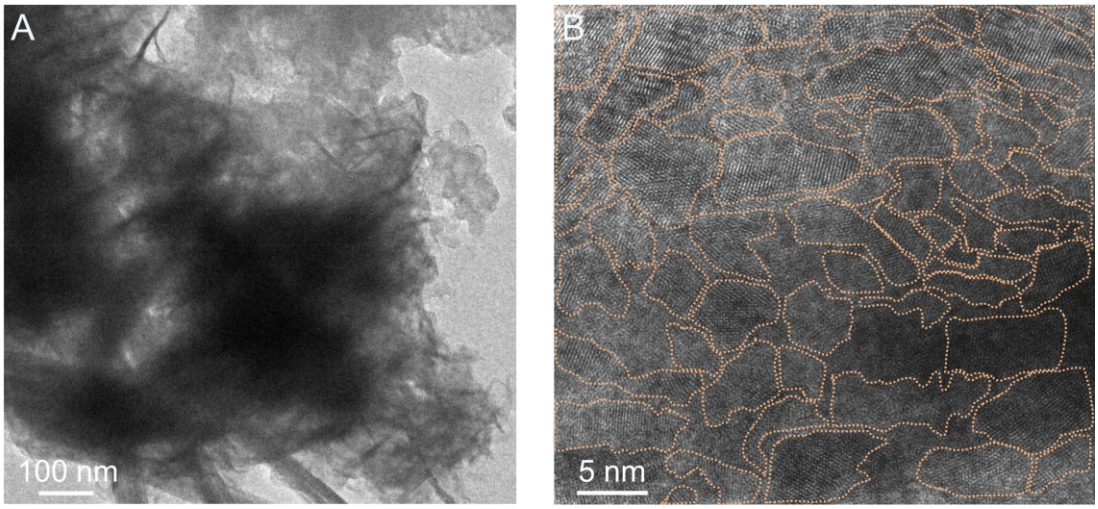

Figure S43. (A) TEM image and (B) HRTEM image of oc-Cu_2O after LSV and CA-15 min treatments.

1 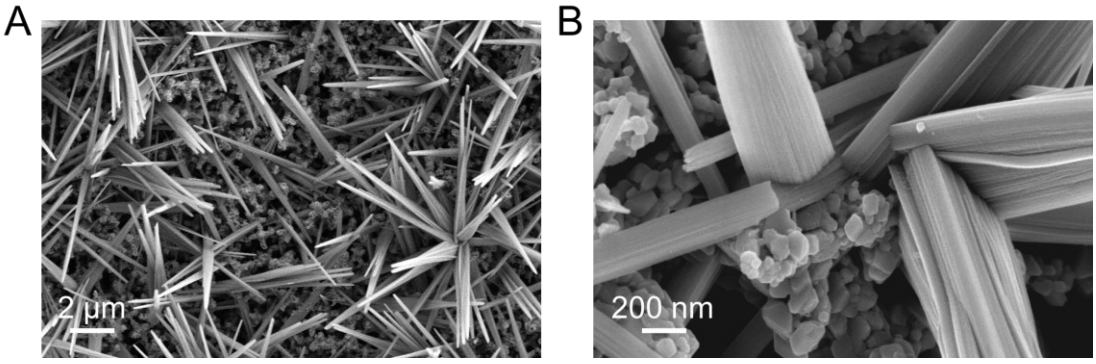

2 Figure S44. (A) Low-magnification and (B) high-magnification SEM images of the oc-

3 Cu_2O material after LSV and CA treatments in an Ar atmosphere.

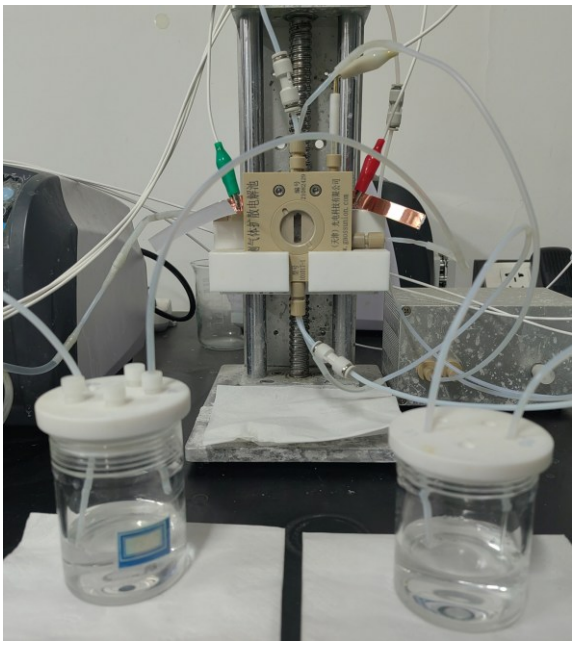

Figure S45. Photograph of flow cell for CO_2RR.

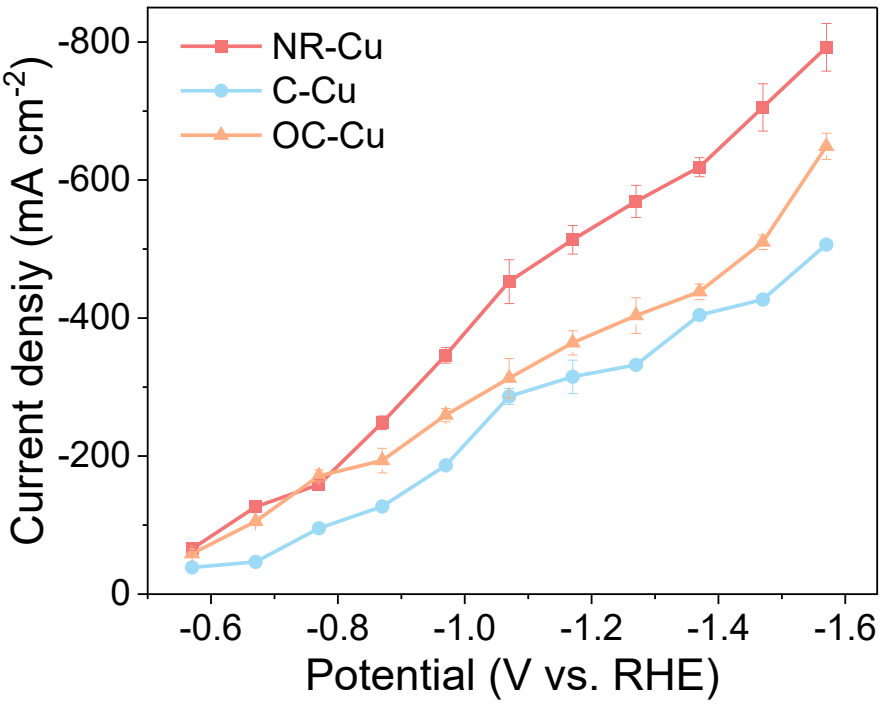

Figure S46. The total current density of NR-Cu, C-Cu and OC-Cu catalysts at different potentials.

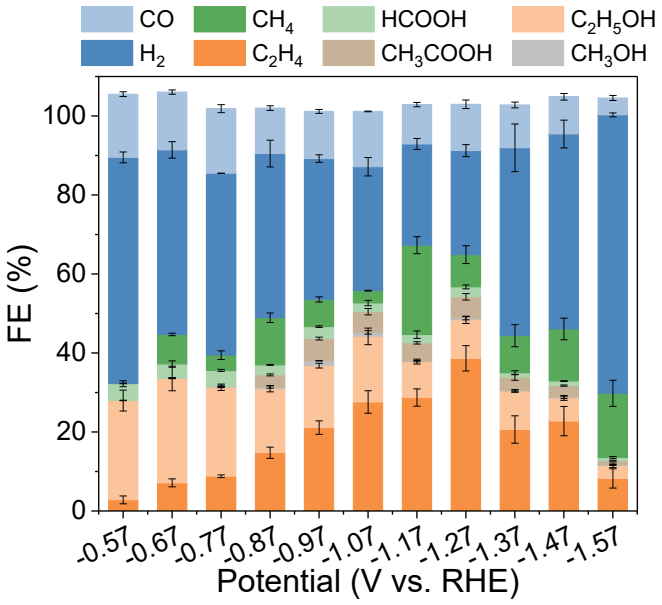

Figure S47. FEs of CO_2RR products at different potentials for C-Cu catalyst.

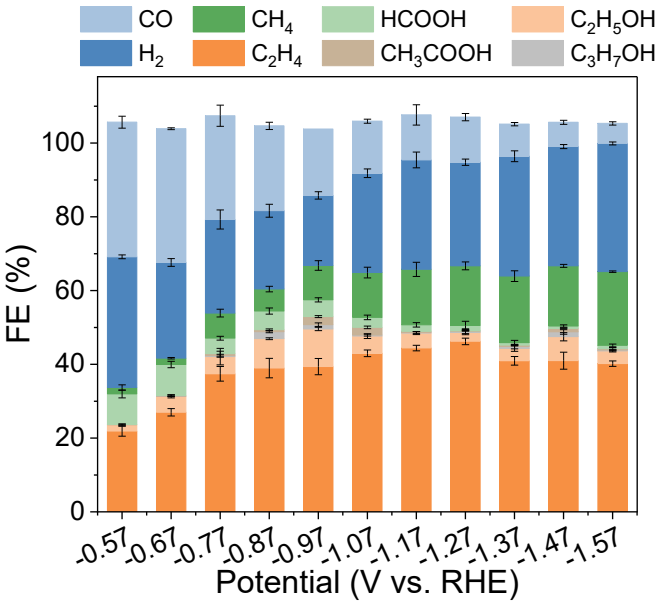

Figure S48. FEs of CO_2RR products at different potentials for OC-Cu catalyst.

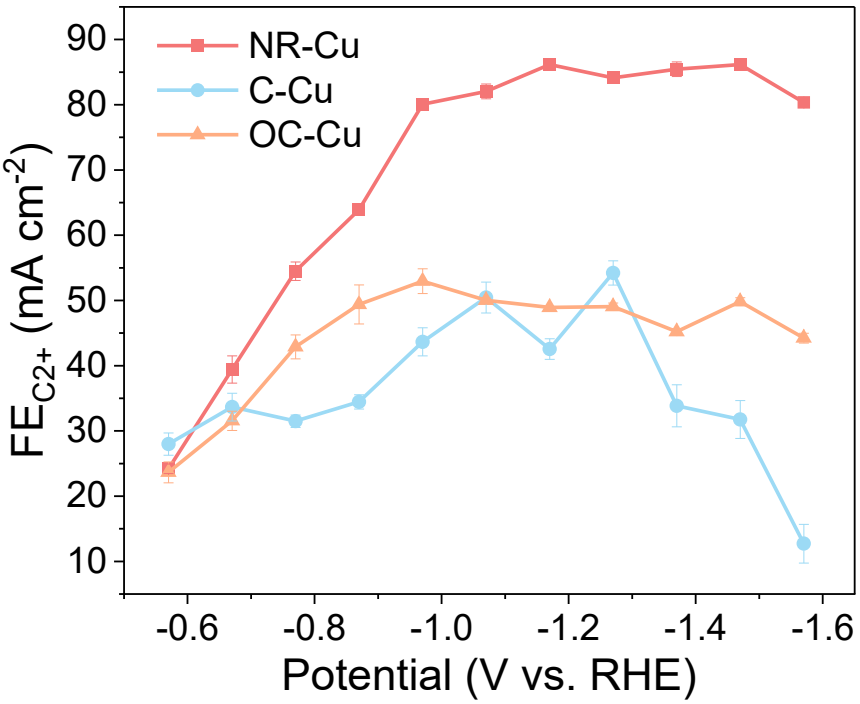

Figure S49. FE_{C2+} of NR-Cu, C-Cu and OC-Cu catalysts at different potentials.

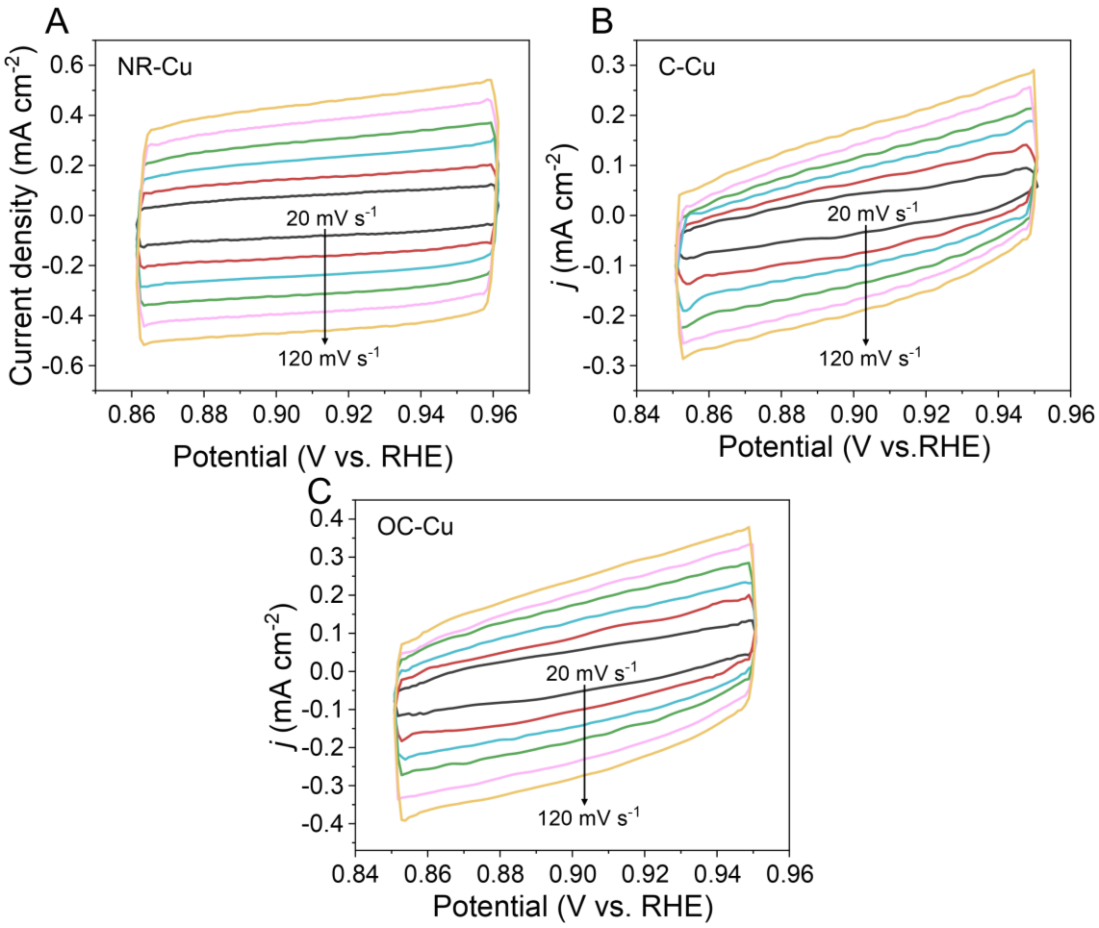

Figure S50. Electrochemical double-layer capacitance measurements. CV curves of (A) NR-Cu, (B) C-Cu and (C) OC-Cu at various scan rates.

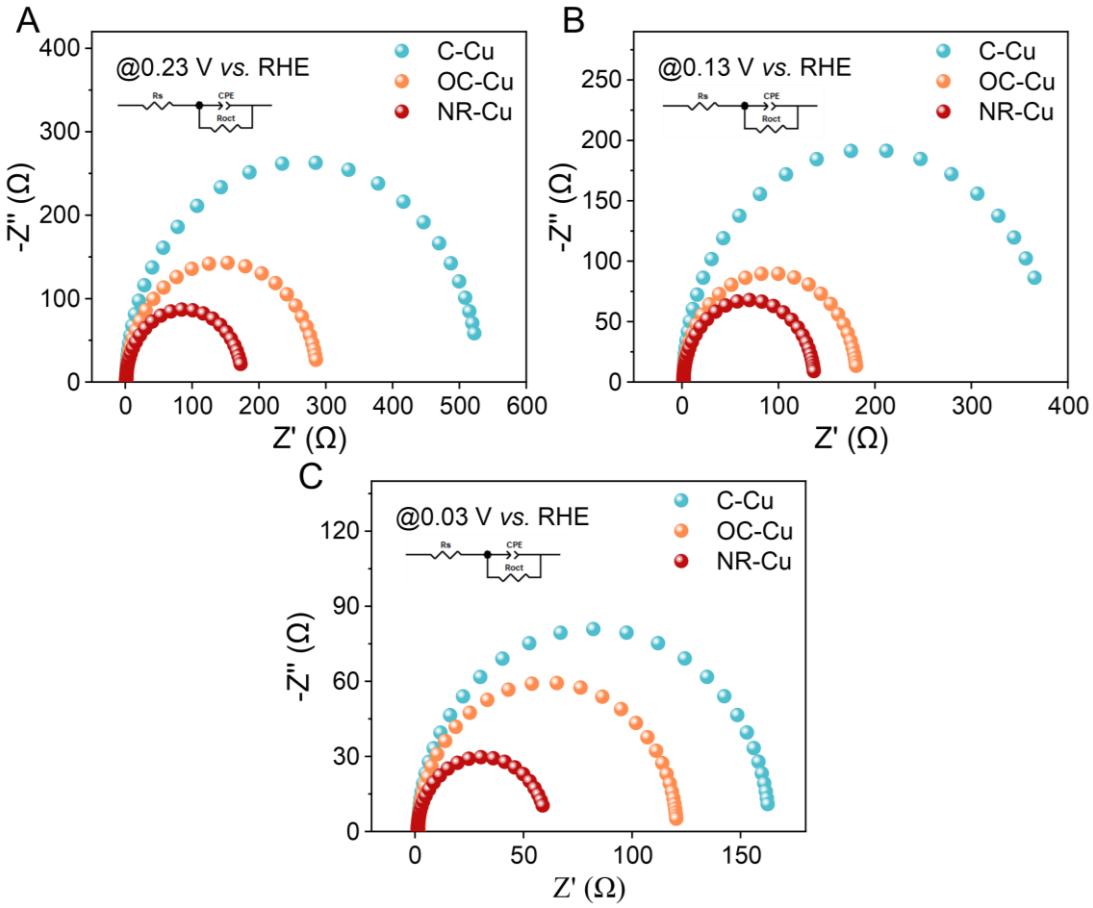

Figure S51. EIS Nyquist plots and equivalent circuits (inset) for NR-Cu, C-Cu and OC-Cu catalysts at different applied potentials.

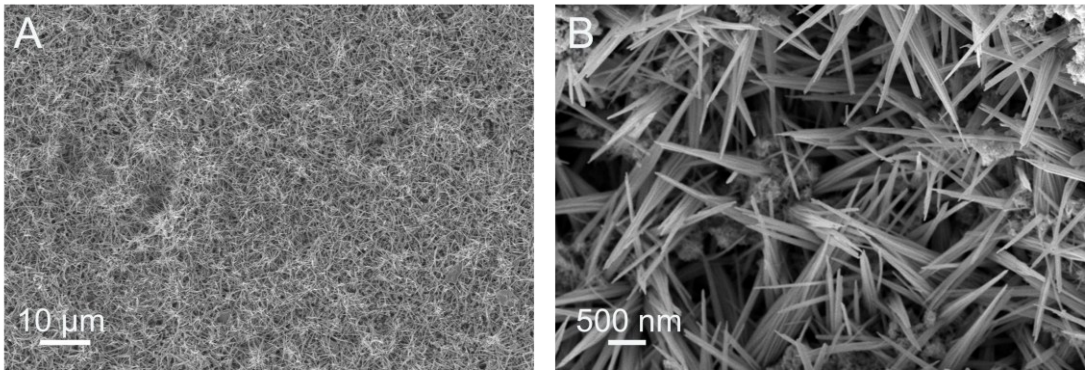

Figure S52. (A) Low-magnification and (B) high-magnification SEM images of NR-Cu catalyst after CO_2RR stability test.

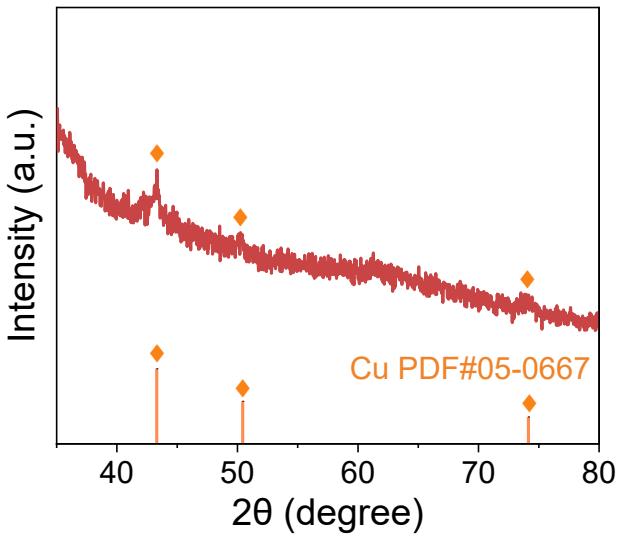

Figure S53. XRD pattern of NR-Cu catalyst after CO_2RR stability test.

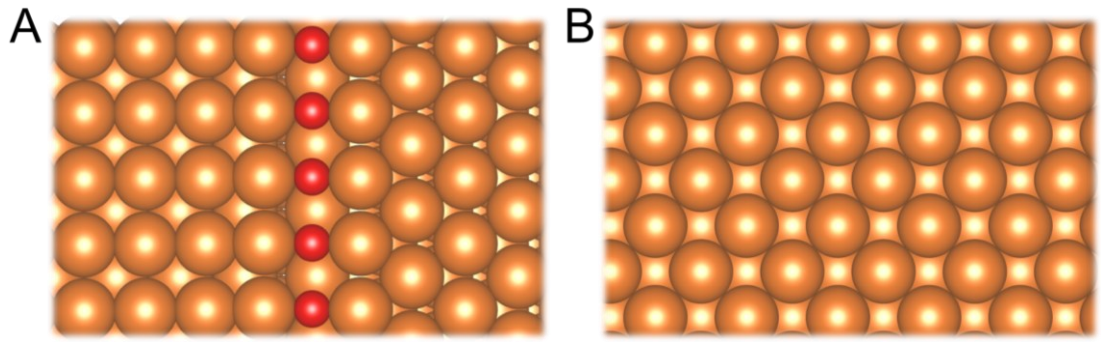

Figure S54. Optimized structures of (A) NR-Cu and (B) C-Cu. Orange and red spheres represent Cu and O atoms, respectively.

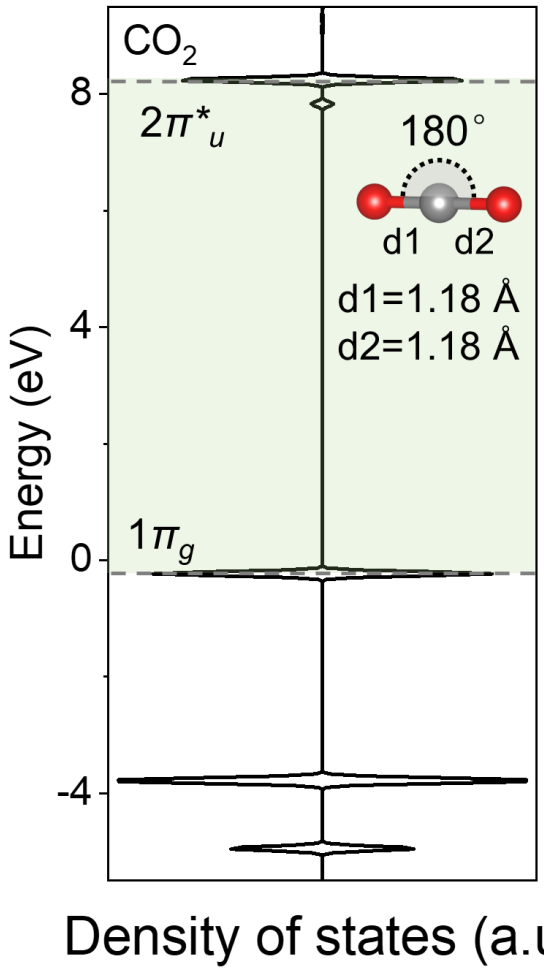

Figure S55. The DOS plots for isolated CO_2 molecule. The dashed lines represent the highest occupied molecular orbital (HOMO) and the lowest unoccupied molecular orbital (LUMO). Gray and red spheres represent C and O atoms, respectively.

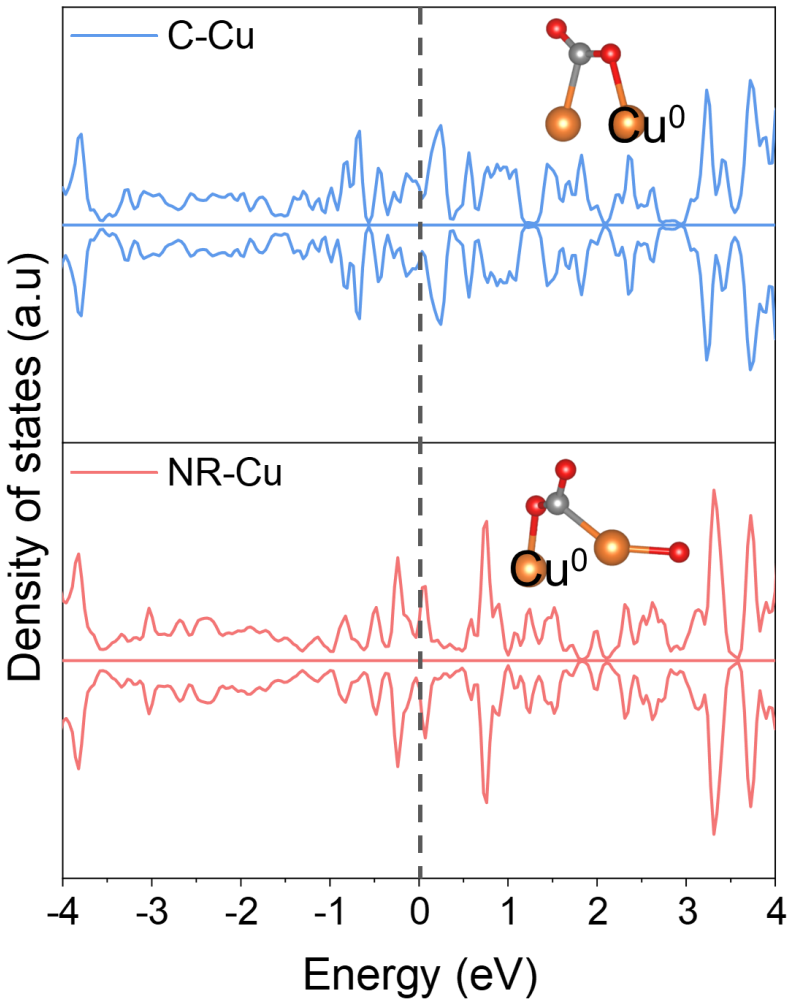

Figure S56. The Cu 1s DOS of C-Cu and NR-Cu with adsorbed CO_2. The Orange, red and gray spheres represent Cu, O and C atoms, respectively.

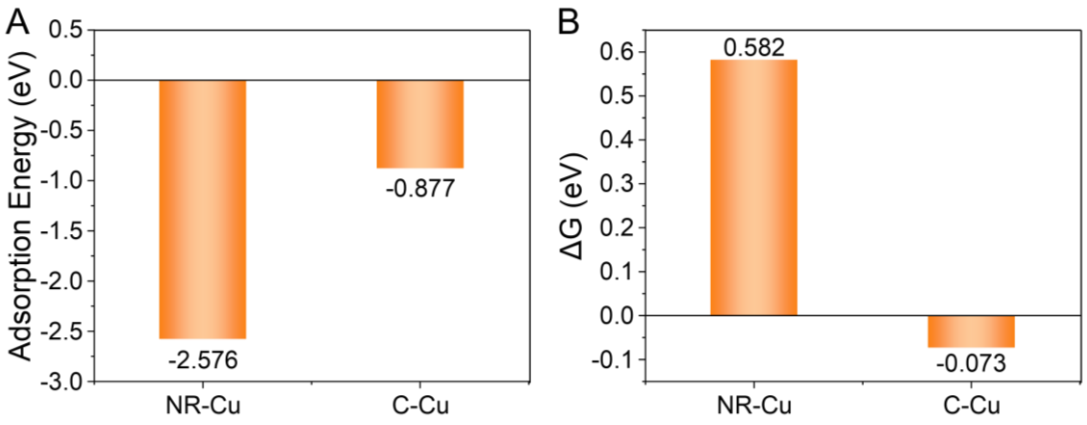

Figure S57. (A) CO adsorption energies on NR-Cu and C-Cu calculated by DFT. (B) ΔG values for the *CO-to-CO pathway on NR-Cu and C-Cu.

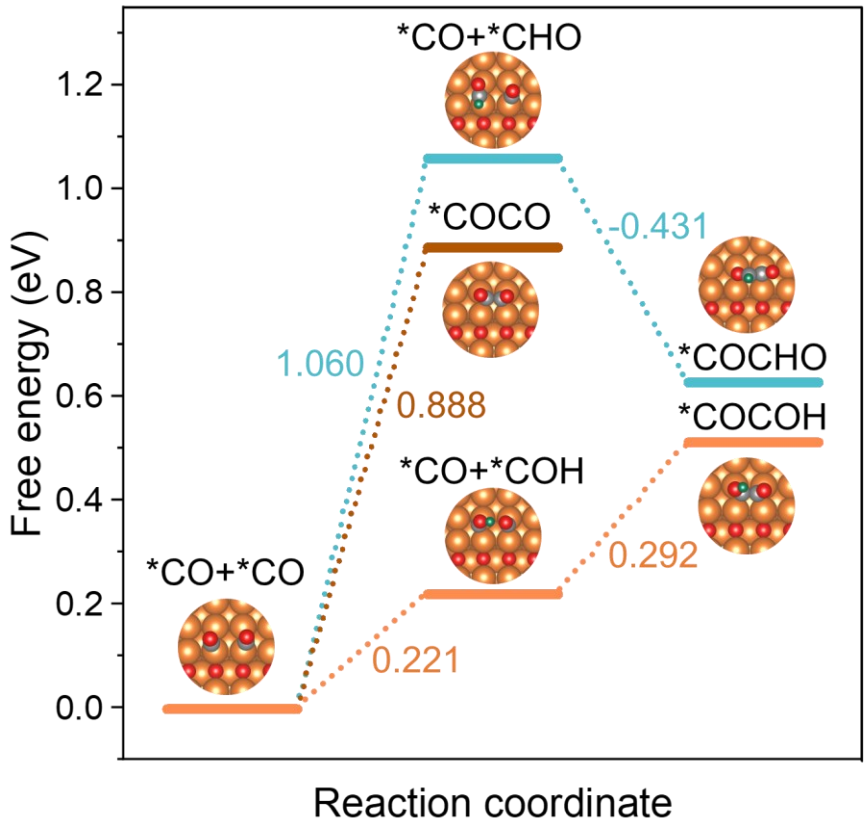

Figure S58. ΔG diagrams for the formation of *COCOH, *COCHO and *COCO on NR-Cu. The Orange, red, green and gray spheres represent Cu, O, H and C atoms, respectively.

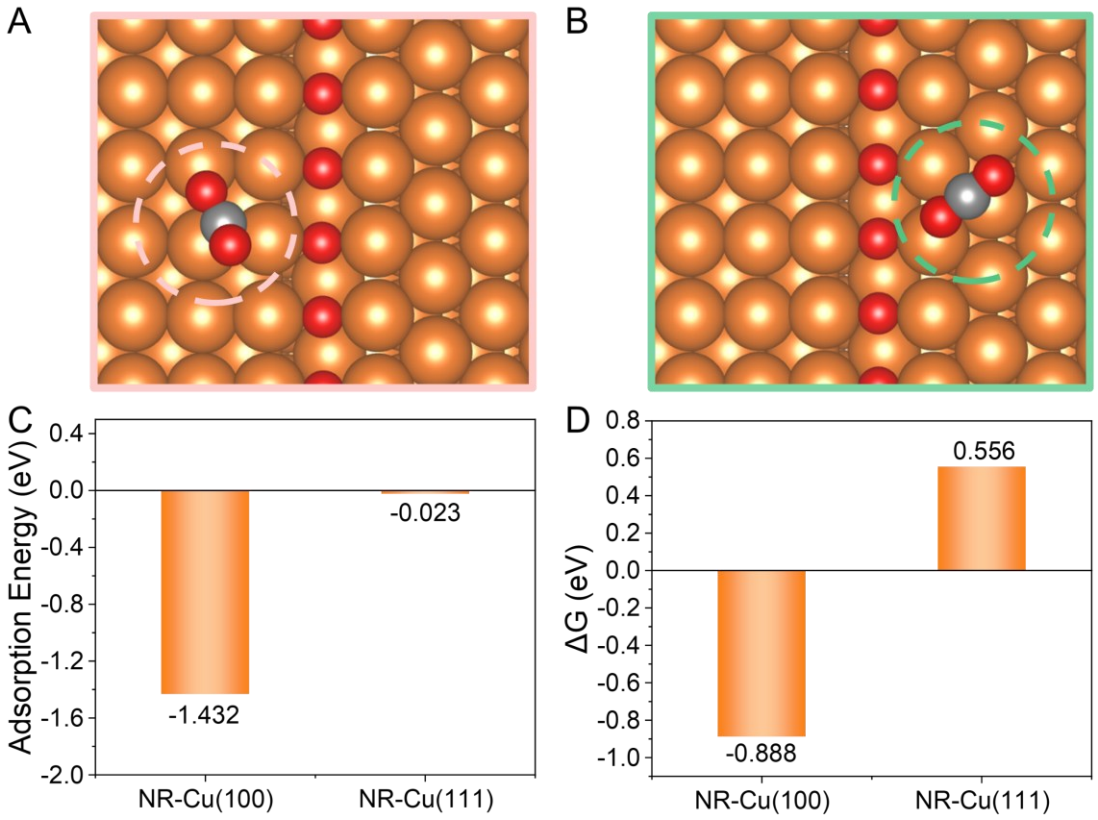

Figure S59. CO_2 adsorption configurations on distinct facets at a NR-Cu grain boundary. (A) NR-Cu(100) and (B) NR-Cu(111). (C) CO_2 adsorption energies for NR-Cu(100) and NR-Cu(111). (D) ΔG values for the CO_2-to-*CO_2 pathway on NR-Cu(100) and NR-Cu(111). The Orange, red and gray spheres represent Cu, O and C atoms, respectively.

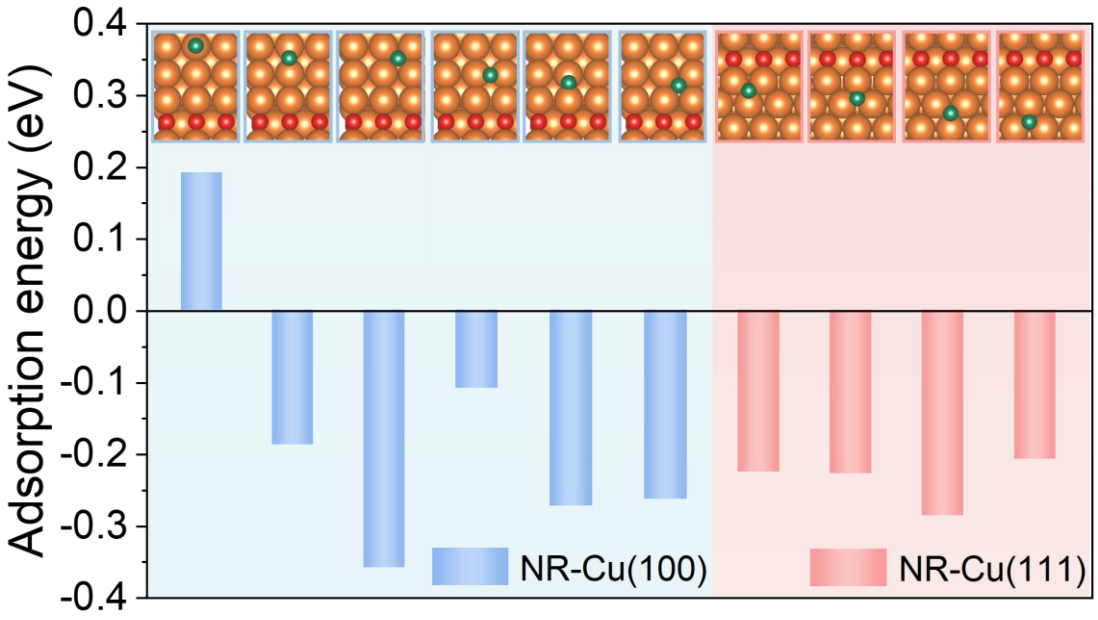

Figure S60. Structural models of hydrogen adsorption on the Cu sites of NR-Cu and hydrogen adsorption energies calculated by DFT. The Orange, red and green spheres represent Cu, O and H atoms, respectively.

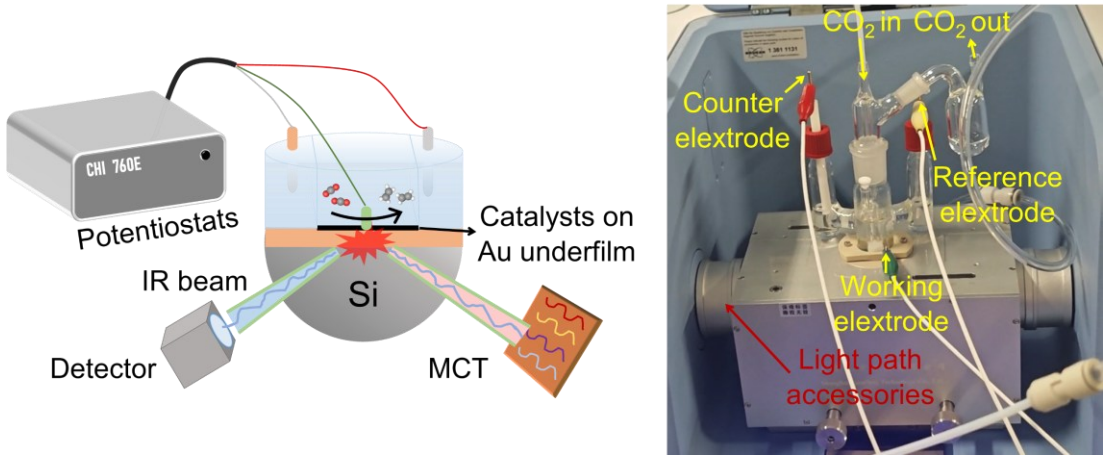

1

2 Figure S61. Schematic diagram (left) and photograph (right) of the *in-situ*
3 electrochemical ATR-SEIRAS measurement.

Supplementary Tables

Table S1. EXAFS fitting parameters extracted from the Cu K-edge (S_0^2 = 0.860).

Sample	Path	CN	R(Å)	$\sigma^2(10^{-3}\times Å^2)$	$\triangle E_0$(eV)	R factor
Cu foil	Cu-Cu	12	2.54±0.01	8.7±0.4	4.7±0.6	0.0038
NR-Cu	Cu-Cu	7.0±0.5	2.54±0.01	9.0±0.7	4.5±0.7	0.0169
C-Cu	Cu-Cu	9.1±0.8	2.54±0.01	9.0±0.8	4.5±0.9	0.0089
OC-Cu	Cu-Cu	8.1±0.3	2.54±0.02	8.5±0.6	4.3±0.8	0.0089

EXAFS fitting results for structural parameters around Cu atoms in Cu foil (R: range from 1 to 3 Å), NR-Cu (R: range from 1.8 to 3 Å), C-Cu (R: range from 1 to 3 Å) and OC-Cu (R: range from 1 to 3 Å). CN stands for coordination number; R stands for bond distance; σ^2 stands for Debye-Waller factor; $\triangle E_0$ stands for edge-energy shift; R factor stands for goodness of fit; S_0^2 is fixed as 0.860 during EXAFS fitting based on the Cu foil reference. Error bounds that characterize the structural parameters obtained by EXAFS spectroscopy were estimated as N±20%.

Table S2. List of assignment of *in-situ* Raman peaks.

Raman shift (cm^{-1})	Assignment	Ref.
~360	ν(Cu-CO)	13
~528, ~617	Cu_2O	14
~525	$\nu(CuO_x/Cu(OH)_y)$	15
~706	ν(Cu-OH)	15,16
~1071	$\nu(*CO_3^{2-})$	17,18
1240-1290	δ(C-H)	19
~1317	$\nu(CO_2^-)/\delta(CO_2)$	17,20,21
~1690	ν(*COOH)	13
~1850	$\nu(Cu\text{-}CO_{bridge})$	14,15
2030-2090	$\nu(Cu\text{-}CO_{top})$	15,18,20

ν: stretching vibration; δ: deformational vibration.

Table S3. The detailed comparison of various reported Cu-based electrocatalysts.

Catalysts	Electrolyzer	Electrolyte	j_{total} (mA cm^{-2})	FE_{C2H4} (%)	j_{C2H4} (mA cm^{-2})	Ref.
Cu_2O derived Cu	H-cell	0.1 M $KHCO_3$	25	40	10	22
Plasma-activated Cu	H-cell	0.1 M $KHCO_3$	23	60	13.8	23
B-doped Cu	H-cell	0.1 M KCl	70	52	36.4	24
(100) Cu nanocubes	H-cell	0.25 M $KHCO_3$	68	32	21.8	25
[a]$Cu(OH)_2$-D/Cu	Flow cell	1 M KOH	250	58	145	26
[b]NPC_{MAF-4}-Cu_2-21	Flow cell	0.1 M $KHCO_3$	180	52	93.6	27
[c]HKUST-1	Flow cell	1 M KOH	262	45	180	28
[d]Cu-S	Flow cell	1 M KOH	398.6	57.2	228	29
[e]Cu_2O(CO)	Flow cell	1 M KOH	500	56.6	283	8
$Cu_2P_2O_7$	Flow cell	1 M KOH	350	41.8	83.6	30
[f]CuO-C(O)	Flow cell	1 M KOH	500	60	300	31
[g]EP-CoP/Cu	Flow cell	1 M KOH	726	43	312.2	32
B-Cu	Flow cell	1 M KOH	200	49	98	33
F-Cu	Flow cell	1M KOH	250	59.9	150	34
Cu_{cub}	Flow cell	1 M KOH	300	57	171	35
[h]Cu-$C_{6\%}$	Flow cell	1 M KOH	800	47	376	36
CuTA	Flow cell	1 M KOH	700	60.8	425.6	37
Cu nanoparticle	Flow cell	1 M KOH	430	35	150.5	38
Dendritic Cu	Flow cell	0.1 M $KHCO_3$	450	36	162	39
25 nm Cu film	Flow cell	10 M KOH	275	66	181.5	40
CuAg-wire	Flow cell	1 M KOH	300	60	180	41
Porous Cu	Flow cell	1 M KOH	653	38.6	252	42

[i]Cu-P1	Flow cell	1 M KOH	450	72	324	43
[j]Cu-CoPc	Flow cell	1 M KOH	420	67	281.5	44
NR-Cu	Flow cell	1 M KOH	514	74.7	384	This work

[a]$Cu(OH)_2$-D/Cu: $Cu(OH)_2$ supported on Cu foil was placed in a CO_2-saturated 0.1 M $KHCO_3$ aqueous solution and reduced under the bias potential of -0.5 V *vs.* RHE for ≈ 800 s

[b]$NPC_{MAF\text{-}4}$-Cu_2-21: Nitrogen-doped porous carbons comprising dual Cu sites at a loading of 21.2 wt%

[c]HKUST-1: a Cu dimer catalyst with paddle-wheel structure in HKUST-1 MOF

[d]Cu-S: the stable Cu@ Smotifis dispersed in the framework of HKUST-1

[e]Cu_2O(CO): a Cu_2O-Cu nanocube hybrid catalyst obtained by the thermal reduction of Cu_2O nanocubes under a CO atmosphere

[f]CuO-C(O): a CuO nanosheet/graphene oxide dots hybrid

[g]EP-CoP/Cu: a nano-thickness cobalt porphyrin polymeric network (EP-CoP) onto a Cu electrode

[h]$Cu\text{-}C_{6\%}$: a carbon-modified Cu catalyst with a carbon atomic percentage of 6%

[i]Cu-P1: a Cu-polyamine hybrid catalyst

[j]Cu-CoPc: a tandem catalyst with cobalt phthalocyanine

Table S4. List of peak assignments for *in-situ* ATR-SEIRAS spectra.

Band center (cm^{-1})	Assignment	Ref.
~1362, ~1125	*OC_2H_5	45-47
1400-1430	*COOH	45,46
1465-1540, ~1717	*COH	46
~1211, ~1584	*OCCOH	45-47
2070-2080	*CO	46
~2854, ~2927	C-H	48

Supplementary References

[1] Shang, Y. & Guo, L. Facet-controlled synthetic strategy of Cu_2O-based crystals for catalysis and sensing. *Adv. Sci.* **2**, 1500140 (2015).

[2] Shang, Y., et al. A facile top-down etching to create a Cu_2O jagged polyhedron covered with numerous {110} edges and {111} corners with enhanced photocatalytic activity. *Chem. Eur. J.* **18**, 14261-14266 (2012).

[3] Yan, et al. Ubiquitous strategy for probing ATR surface-enhanced infrared absorption at platinum group metal-electrolyte interfaces. *J. Phys. Chem. B* **109**, 7900-7906 (2005).

[4] Kresse, G. & Furthmüller, J. Efficiency of ab-initio total energy calculations for metals and semiconductors using a plane-wave basis set. *Compu. Mater. Sci.* **6**, 15-50 (1996).

[5] Blöchl, P. E. Projector augmented-wave method. *Phys. Rev. B* **50**, 17953-17979 (1994).

[6] Perdew, J. P., et al. Atoms, molecules, solids, and surfaces: Applications of the generalized gradient approximation for exchange and correlation. *Phys. Rev. B* **46**, 6671-6687 (1992).

[7] Nørskov, J. K., et al. Origin of the overpotential for oxygen reduction at a fuel-cell cathode. *J. Phys. Chem. B* **108**, 17886-17892 (2004).

[8] Wu, Q., et al. Nanograin-boundary-abundant Cu_2O-Cu nanocubes with high C_{2+} selectivity and good stability during electrochemical CO_2 reduction at a current density of 500 mA cm^{-2}. *ACS Nano* **17**, 12884-12894 (2023).

[9] Wang, Y., et al. Synthesis of porous Cu_2O/CuO cages using Cu-based metal-organic frameworks as templates and their gas-sensing properties. *J. Mater. Chem. A* **3**, 12796-12803 (2015).

[10] Wang, L., et al. Stabilized $Cu^{\delta+}$-OH species on in situ reconstructed Cu nanoparticles for CO_2-to-C_2H_4 conversion in neutral media. *Nat. Commun.* **15**, 7477 (2024).

[11] Artiglia, L., et al. In situ X-ray photoelectron spectroscopy detects multiple active sites involved in the selective anaerobic oxidation of methane in copper-exchanged zeolites. *ACS Catal.* **9**, 6728-6737 (2019).

[12] Dan, Z., Yang, Y., Qin, F., Wang, H. & Chang, H. Facile fabrication of Cu_2O nanobelts in ethanol on nanoporous Cu and their photodegradation of methyl orange. *Materials* **11**, 446 (2018).

[13] Zhang, W., et al. Crystallinity-directed in situ reconstruction of Cu-Al oxides yielding tunable $Cu^{\delta+}$ sites for electrochemical CO_2-to-C_{2+} conversion. *ACS Nano* **19**, 24023-24033 (2025).

[14] Chang, X., Zhao, Y. & Xu, B. pH dependence of Cu surface speciation in the electrochemical CO reduction reaction. *ACS Catal.* **10**, 13737-13747 (2020).

[15] Zhao, Y., et al. Speciation of Cu surfaces during the electrochemical CO reduction reaction. *J. Am. Chem. Soc.* **142**, 9735-9743 (2020).

[16] Bodappa, N., et al. Early stages of electrochemical oxidation of Cu(111) and polycrystalline Cu surfaces revealed by in Situ Raman spectroscopy. *J. Am. Chem. Soc.* **141**, 12192-12196 (2019).

[17] Chernyshova, I. V., Somasundaran, P. & Ponnurangam, S. On the origin of the elusive first intermediate of CO_2 electroreduction. *Proc. Natl. Acad. Sci.* **115**, E9261-E9270 (2018).

[18] Ma, L., et al. Cu supraparticles with enhanced mass transfer and abundant C-C coupling sites achieving ampere-level CO_2-to-C_{2+} electrosynthesis. *Nat. Commun.* **16**, 3421 (2025).

[19] Fant, K. & Boggs, J. E. Theoretical prediction of vibrational spectra: the harmonic force field and the vibrational spectrum of 4-methylpyridine. *Tetrahedron* **42**, 1265-1274 (1986).

[20] Niu, Z.-Z., et al. Hierarchical copper with inherent hydrophobicity mitigates electrode flooding for high-Rate CO_2 electroreduction to multicarbon products. *J. Am. Chem. Soc.* **143**, 8011-8021 (2021).

[21] Santos Jr, V. O., Leite, I. R., Brolo, A. G. & Rubim, J. C. The electrochemical reduction of CO_2 on a copper electrode in 1-n-butyl-3-methyl imidazolium tetrafluoroborate (BMI.BF4) monitored by surface-enhanced Raman scattering (SERS). *J. Raman Spectrosc.* **47**, 674-680 (2016).

[22] Ren, D., et al. Selective electrochemical reduction of carbon dioxide to ethylene and ethanol on copper(I) oxide catalysts. *ACS Catal.* **5**, 2814-2821 (2015).

[23] Mistry, H., et al. Highly selective plasma-activated copper catalysts for carbon dioxide reduction to ethylene. *Nat. Commun.* **7**, 12123 (2016).

[24] Zhou, Y., et al. Dopant-induced electron localization drives CO_2 reduction to C_2 hydrocarbons. *Nat. Chem.* **10**, 974-980 (2018).

[25] Jiang, K., et al. Metal ion cycling of Cu foil for selective C-C coupling in electrochemical CO_2 reduction. *Nat. Catal.* **1**, 111-119 (2018).

[26] Zhong, D., et al. Coupling of Cu(100) and (110) facets promotes carbon dioxide conversion to hydrocarbons and alcohols. *Angew. Chem. Int. Ed.* **60**, 4879-4885 (2021).

[27] Heng, J.-M., Zhu, H.-L., Zhao, Z.-H., Liao, P.-Q. & Chen, X.-M. Fabrication of ultrahigh-loading dual copper sites in nitrogen-doped porous carbons boosting electroreduction of CO_2 to C_2H_4 under neutral conditions. *Adv. Mater.* **37**, 2415101 (2025).

[28] Nam, D.-H., et al. Metal-organic frameworks mediate Cu coordination for selective CO_2 electroreduction. *J. Am. Chem. Soc.* **140**, 11378-11386 (2018).

[29] Wen, C. F., et al. Highly ethylene-eelective electrocatalytic CO_2 reduction enabled by isolated Cu-S motifs in metal-organic framework based precatalysts. *Angew. Chem. Int. Ed.* **61**, e202111700 (2022).
[30] Sang, J., et al. A reconstructed $Cu_2P_2O_7$ catalyst for selective CO_2 electroreduction to multicarbon products. *Angew. Chem. Int. Ed.* **61**, e202114238 (2022).
[31] Du, R., et al. Cu-C(O) interfaces deliver remarkable selectivity and stability for CO_2 reduction to C_{2+} products at industrial current density of 500 mA cm^{-2}. *Small* **19**, 2301289 (2023).
[32] Wang, C., et al. In Situ electropolymerizing toward EP-CoP/Cu tandem catalyst for enhanced electrochemical CO_2-to-ethylene conversion. *Adv. Sci.* **11**, 2404053 (2024).
[33] Song, Y., et al. B-Cu-Zn gas diffusion electrodes for CO_2 electroreduction to C_{2+} products at high current densities. *Angew. Chem. Int. Ed.* **60**, 9135-9141 (2021).
[34] Zhou, Z., Hu, X., Li, J., Xie, H. & Wen, L. Enhanced CO_2 electroreduction to multi-carbon products on copper via plasma fluorination. *Adv. Sci.* **11**, 2309963 (2024).
[35] De Gregorio, G. L., et al. Facet-dependent selectivity of Cu catalysts in electrochemical CO_2 reduction at commercially viable current densities. *ACS Catal.* **10**, 4854-4862 (2020).
[36] Dong, X., et al. Electrochemical CO_2 reduction to C_{2+} products with ampere-level current on carbon-modified copper catalysts. *Acta Phys. -Chim. Sin.* **41**, 100024 (2025).
[37] Wu, M., et al. Sequential *CO management via controlling in situ reconstruction for efficient industrial-current-density CO_2-to-C_{2+} electroreduction. *Proc. Natl. Acad. Sci.* **120**, e2302851120 (2023).
[38] Ma, S., et al. One-step electrosynthesis of ethylene and ethanol from CO_2 in an alkaline electrolyzer. *J. Power Sources* **301**, 219-228 (2016).
[39] De Luna, P., et al. Catalyst electro-redeposition controls morphology and oxidation state for selective carbon dioxide reduction. *Nat. Catal.* **1**, 103-110 (2018).
[40] Dinh, C.-T., et al. CO_2 electroreduction to ethylene via hydroxide-mediated copper catalysis at an abrupt interface. *Science* **360**, 783-787 (2018).
[41] Hoang, T. T. H., et al. Nanoporous copper-silver alloys by additive-controlled electrodeposition for the selective electroreduction of CO_2 to ethylene and ethanol. *J. Am. Chem. Soc.* **140**, 5791-5797 (2018).
[42] Lv, J.-J., et al. A highly porous copper electrocatalyst for carbon dioxide reduction. *Adv. Mater.* **30**, 1803111 (2018).
[43] Chen, X., et al. Electrochemical CO_2-to-ethylene conversion on polyamine-incorporated Cu electrodes. *Nat. Catal.* **4**, 20-27 (2021).
[44] Kong, X., et al. Understanding the effect of *CO coverage on C-C coupling toward CO_2 electroreduction. *Nano Lett.* **22**, 3801-3808 (2022).
[45] Zheng, M., et al. Electrocatalytic CO_2-to-C_{2+} with ampere-level current on heteroatom-engineered copper via tuning *CO intermediate coverage. *J. Am. Chem. Soc.* **144**, 14936-14944 (2022).
[46] Zhang, T., Yuan, B., Wang, W., He, J. & Xiang, X. Tailoring *H intermediate coverage on the $CuAl_2O_4$/CuO catalyst for enhanced electrocatalytic CO_2 reduction to ethanol. *Angew. Chem. Int. Ed.* **62**, e202302096 (2023).
[47] Yin, Y., et al. Enhancing CO_2 electroreduction to ethylene in acidic solution by optimizing cation configuration on the Cu surface. *J. Am. Chem. Soc.* **147**, 25584-25591 (2025).
[48] Wei, D., et al. Surface adsorbed hydroxyl: A double-edged sword in electrochemical CO_2 reduction over oxide-derived copper. *Angew. Chem. Int. Ed.* **62**, e202306876 (2023).